Seismic bulk and shear attenuation along a transect from Kama‘ehuakanaloa volcano through Mauna Loa to the Aloha Cabled Observatory: Implications for the distribution of partial melt

Rhett Butler[1]

[1]Hawai‘i Institute for Geophysics and Planetology, School of Ocean and Earth Science and Technology, University of Hawai‘i at Mānoa, 1680 East-West Road, POST 602, Honolulu, HI 96822.

HIGP Technical Report 2494, June, 2024, pp54. https://doi.org/10.21203/rs.3.rs-4548134/v1

ORCiD 0000-0002-1796-2797

Key points

- Bulk attenuation exceeds shear attenuation for all Hawai‘i earthquakes observed
- A thermodynamic equilibrium model of partial melt effectively fits a bulk attenuation data set for Mauna Loa and Kama‘ehuakanaloa volcanos
- Aloha Cabled Observatory successfully recorded all Q_K and Q_S data from Mauna Loa and Kama‘ehuakanaloa volcanos using a single hydrophone

ABSTRACT

Bulk (Q_K) and shear (Q_S) attenuation are measured and modeled to ~50 km depth beneath Hawai‘i. High-frequency (>50 Hz) earthquakes are routinely observed from the Aloha Cabled Observatory (ACO) along the azimuth to Mauna Loa, Pāhala, and Kama‘ehuakanaloa volcano. Bulk attenuation is consistently larger than shear attenuation beneath Hawai‘i at frequencies >2 Hz. The Mauna Loa Summit shows the smallest Q values, and transects approaching the Summit from the southeast differ asymmetrically with those departing to the northwest from the Summit. Transect maps of Q are created from the measurements to present in plan view the distribution of Q_K and Q_S near the moho. Activation energy E^* models of Q_S are tested both at Pāhala and Kama‘ehuakanaloa for experimentally determined olivine E^* using the temperature derived from a Hawai‘i Hotspot geotherm and pressure. The Q_K arising from water-filled pores in vesicular basalts within the shallow oceanic crust are a hypothesized mechanism for bulk attenuation measured in the shallow crust near ACO and Wake Island. Below the shallow oceanic crust, partial melt presents a feasible bulk attenuation mechanism at volcanos. Fitting a thermodynamic equilibrium model for frequencies >1 Hz to the Q_K measurements shows a very good match to the Q_K data, predicting partial melt fractions of 0.1% to 10%. Translating the Q maps into partial melt regions near Mauna Loa, Pāhala, and Kama‘ehuakanaloa volcano gives a first view of the observation, location, and distribution of partial melt along the ~100 km transect from southeast to northwest of Mauna Loa.

Plain Language Summary

Attenuation of seismic energy in Hawai‘i has two separate mechanisms: bulk compression/decompression and shearing the rock. These attenuation properties are measured from earthquakes along a line from the Aloha Cabled Observatory (ACO) to Mauna Loa, and southeast to Pāhala, and Kama‘ehuakanaloa volcano. These earthquakes occur down to ~50 km depth, and are rich in high frequency energy. Bulk attenuation is uniformly larger than shear attenuation in Hawai‘i. The Mauna Loa Summit shows the largest attenuation observed. Traversing the Summit from the southeast, attenuation is not symmetrical with paths traversing to the northwest from the Summit. For shallow and deep earthquakes, experimentally determined olivine mineral properties compare successfully with observed shear attenuation measurements. Partial melting of rock at a boundary in contact with magma presents a feasible bulk attenuation mechanism at volcanos. Fitting a partial melting model to the bulk attenuation measurements shows a very good match to the data, predicting partial melt fractions of ~1% volume. Translating the bulk attenuation maps into partial melt regions near Mauna Loa gives a first view of the location and distribution of partial melt along the ~100 km traverse from southeast to northwest of Mauna Loa.

Index terms [3050, 5144, 7280, 3619, 3909]

Keywords [bulk attenuation Mauna Loa partial melt]

1 INTRODUCTION

This study was first motivated by the swarm of 50 M_w 5+ earthquakes which occurred during the collapse of the Kīlauea caldera in 2018 (e.g., Butler 2019, Neal et al., 2019). Stacking the Kīlauea data at seismic stations situated along the azimuth to the Aloha Cabled Observatory (ACO), Butler (2020) derived effective Q (Q_{eff}) of bulk and shear attenuation for the paths beneath the volcanos and within the oceanic crust (Figure 1). In addition to the frequency dependent effective Q_{eff} values, shear attenuation activation energy, E^*, for the shallow basaltic crust was derived. Except for the nearest Kīlauea site, where $Q_S \sim Q_K$ at < 10 Hz, the measured $Q_S > Q_K$ for the Kīlauea data, and a mechanism for the observed bulk attenuation was hypothesized. This paper and its predecessor further serve to acknowledge and highlight the remarkable scientific capabilities of cabled seafloor observatories, even when employing only a *single high-frequency seafloor hydrophone*.

A swarm of 16 $M_L \gtrsim 4$ deep earthquakes (>30 km) in 2020–2023 near Pāhala on the southeast coast of Hawai‘i Island were reported by the U.S. Geological Survey – Hawaiian Volcano Observatory (USGS-HVO). These earthquakes offered a similar geometric arrangement transecting Mauna Loa to that of the Butler (2020) Kīlauea study. Earthquake spectrograms were reviewed for the Pāhala events, and other earthquakes along the azimuths between ACO and Mauna Loa, Pāhala, & Kama‘ehuakanaloa (Figure A1).

The narrow study corridor is presented in Figure 1 [Left] extending from ACO to Mauna Loa, Kama‘ehuakanaloa, and Pāhala, and from ACO to Kīlauea. Figure 1 [Right] shows the epicentral locations of earthquake in the data set. The mean, very shallow, hypocentral depths for the Kīlauea and Mauna Loa caldron earthquakes are 0.3 and -0.2 km, respectively, and hence broadly analogous. The paths have comparable propagation distances and azimuths to ACO, and the propagation paths merge together approaching ACO. As the propagation path from the Pāhala events transited the crust and below the moho beneath the caldera of Mauna Loa, the swarm affords a comparison of attenuation from the 2018 Kīlauea data. Fortuitously, the azimuth between ACO and Pāhala lay within 1° of the azimuth to Kama‘ehuakanaloa volcano (formerly, Lō‘ihi). The Kama‘ehuakanaloa earthquakes (at depths near 11 km and at 46 km) also exhibited high frequency, deep *S*-waves ~55 Hz (Figure A1).

In Figure 2 [Left], I present the initial measurements and comparison of Q_K and Q_S for Mauna Loa and Kīlauea calderas, following the methodology of Butler (2020). For both volcanos, $Q_S > Q_K$, i.e., bulk attenuation exceeds that for shear attenuation. Moreover, along the path to ACO, the Mauna Loa paths are more attenuating than observed for Kīlauea. The higher frequency content of the Kīlauea *Q* as compared to Mauna Loa may be attributed to larger earthquake sources in the Kīlauea caldera (Kīlauea Mw ~ 5.3 and Mauna Loa M_L ~ 4.2) and lower signal-to-noise (SNR). The effective *Q* measured at ACO from earthquakes southeast of Mauna Loa and transiting the summit is plotted from both shallow and deep events (Figure 2 [Right]), see caption).

Within the MaunaLoa – Kama‘ehuakanaloa volcano edifices I use the multiple earthquakes to separate and identify Q_K and Q_S as a function of frequency for subdivided pathways extending from Mauna Loa–Pāhala–Kama‘ehuakanaloa to ACO. Since Q_S is an exponentially activated process, I confirm that the mapping of experimentally derived activation energies E^* for olivine using a Hawai‘i Hotspot geotherm (Lee et al., 2009) and pressure (PREM, Dziewonski and Anderson, 1981) can appropriately match the change in Q_S between shallow and deep earthquakes both for Pāhala and Kama‘ehuakanaloa.

For Q_K I review physical mechanisms for bulk attenuation (considered in Butler, 1987, 2020) based upon a hypothesis that Q_K viewed near Wake Island and Kīlauea may arise in the oceanic crust due to water filled vesicles in basalt. The observation of significant Q_K where the basalt characteristics are not applicable (e.g., gabbroic basal crust, or olivine below moho) are now considered in the context of partial melting beneath the Mauna Loa region. To model the observed characteristics of $Q_K(f)$, I have employed a thermodynamic equilibrium model of partial melt (Lyakhovsky et al., 2021) to map the $Q_K(f)$ values for a medium characterized with spherical mineral cells (r = 0.5 to 50 mm) each hosting a partial melt fractional (0.1% to 10%) inclusion. By application of the Lyakhovsky et al., (2021) model, I can expand our map of Q_K in the vicinity of Maua Loa into a map of the distribution of partial melt at depths near the moho and deeper near Mauna Loa. Comparing the relocated seismicity of Matoza et al. (2020) and “deep learning” approach of (Wilding et al, 2022) with bulk attenuation transects, I hypothesize that a low-seismicity gap (15–30 km depth) near Pāhala may be associated with observed Q_K due to partial melt.

2 EARTHQUAKE DATASET

I selected earthquakes with $M_L \gtrsim 4$ observed at the ACO between 2011 and 2023 with propagation paths transiting beneath Mauna Loa volcano. These 30 primary events (Table A1) were located along the ACO back azimuth (~145°) including the offshore Kama‘ehuakanaloa volcano and a deep earthquake swarm near Pāhala on the southeast coast of Hawai‘i. Locations of events subsequent to the ACO start date were taken from earthquake relocations (2011–2018, Matoza et al., 2020), and from the Hawaiian Volcano Observatory network thereafter. Five deep secondary offshore events (back azimuths 143°–148°) were also reviewed in the Appendix as a framework to assess unusual earthquake characteristics within the primary event pool. Earthquakes were classified as ‘shallow’ (<12 km) and ‘deep’ (>30 km) based upon depth. The map of events is shown in Figure 1.

The ACO hydrophone data are down sampled from its native 96 KHz to 400 Hz, which captures the full fidelity of the earthquakes. The ACO hydrophone sensor has been calibrated to a Paroscientific nano-resolution Digiquartz® pressure gauge in the overlapping frequency band 1–10 Hz. The hydrophone pressure data are converted into far-field displacement, $u(x, t)$, from which the amplitude spectrum $A(f)$ is derived. *P*- and *S*-wave arrival times are hand-picked and analyzed within the 6.3 sec window between the wave arrival and its first multiple reflection, *PwP,* characteristic of the ACO sensor at 4728 m depth. The spectral analysis of the *P* and *S* windows employed the multitaper method (Park et al, 1987).

2.1 Earthquake sources

I follow the methodology of Butler (2018, 2020) and many prior earthquake source studies (e.g., Aki, 1967; Brune, 1970, Madariaga, 1976,1977; Shearer et al. 2006, Kaneko & Shearer, 2014, 2015) and Hawai‘i attenuation studies (e.g., Scherbaum & Wyss 1990; Hansen et al. 2004; Lin et al. 2015) for estimating Q_{eff} from the offset of the observed spectral slope of the earthquake source from its theoretical, angular frequency fall-off rate, ω^{-2}. The earthquake sources were each carefully examined to ensure conformity with the assumptions of the ω^{-2} (or f^{-2}) source model in the frequency band of the Q_{eff} measurement beyond a measured corner frequency, f_c. No presumption was made regarding the frequency dependence of Q. Figure A2 presents the methodology for measuring Q from the spectral data. Nonconforming sources were observed for a several deep (> 30 km) earthquakes—these are considered in Figures A2 & A3.

For earthquakes north of Moloka‘i observed from ACO (Butler 2018), a low-frequency spectral decay rate of ω^{-2} is observed that steepens to ω^{-4} beyond 50 Hz. Observations of the same are noted in Figure A2.

The earthquake spectrum $u(f)$ is modeled following Kaneko and Shearer (2014)

$$u(f) = \frac{\Omega_0}{1 + (f/f_c)^2} \quad (1)$$

where Ω_0 is the long-period spectral amplitude proportional to seismic moment, M_0, and the spectral fall-off of the source is proportional to f^{-2}. Ω_0 includes frequency independent effects such as geometric spreading, source radiation, and site impedance. The amplitude spectrum is modeled as the product of the source with the effective attenuation,

$$A(x,f) = u(f)\, e^{\frac{-\pi f x}{Q v}} \quad (2)$$

Solving for $Q(f > f_c)$,

$$Q(f) = \frac{\pi f x}{v\,[\log u(f) - \log A(f)]} \quad (3)$$

where x is distance in km and v is the wave velocity, km/s.

Whereas the 2018 Kīlauea earthquake swarm was comprised by nearly identical mechanisms at very shallow depths (<1.4 km), this study is comprised by earthquakes of varying magnitude (3.9–5.3) and depth. Kaneko and Shearer (2015) noted in earthquake source simulations of potentially significant variations in apparent slope and corner frequency as a function of rupture velocity, azimuth, and colatitude from the fault surface.

3 ATTENUATION METHODOLIGY

Attenuation quality factors, Q_P and Q_S, are determined respectively from the *P* and *S* wave data. Q = (E, energy of seismic wave) ÷ (ΔE, energy lost during one cycle of wave) = 2πE/ΔE. Shear waves attenuate due to a complex shear modulus, μ, arising from the shear wave velocity $V_S = \sqrt{\frac{\mu}{\rho}}$, ρ is density, and $Q_S \equiv Q_\mu$. Compressional waves experience losses both in shear (μ) and incompressibility (K) moduli, where $V_P = \sqrt{\frac{K+4\mu/3}{\rho}}$. The attenuation quality factor, Q, is the ratio of the Imaginary (*Im*) to Real (*Re*) parts of the complex moduli (shear μ or bulk K), i.e., $Q_K = \frac{Im(K)}{Re(K)}$ and $Q_\mu = \frac{Im(\mu)}{Re(\mu)}$. The relationship between Q_P, Q_μ, and Q_K is (Anderson, 1989)

$$Q_p^{-1} = LQ_\mu^{-1} + (1-L)Q_K^{-1} \qquad (4)$$
$$L = (4/3)(V_s/V_p)^2$$

Each earthquake propagation path extends to ACO. The attenuation observed at ACO from the NW event (Figure 1) may be effectively removed from the attenuation observed from more distant earthquakes along the same azimuth. For multiple events near a common site (e.g., Pāhala), the values for Q_P and Q_S are stacked, a median filter is applied, and Q_K is determined over the frequency band common to Q_P and Q_S

A transect of Mauna Loa from Pāhala to the NW event may be determined by subtracting the contribution of the NW event from the Pāhala event. To accomplish this, consider the accumulative $t*$ (e.g., Cormier, 1982):

$$t^* = \int_{path} \frac{dt}{Q} \approx \sum_i \frac{\Delta t_i}{Q_i} \qquad (5)$$

The t^* for the whole path is the cumulative t_i^* for the i path segments, where Δt_i is the path segment travel time.

$$t^*_{Pahala \to NW} + t^*_{NW \to ACO} = t^*_{Pahala \to ACO} \qquad (6)$$

$$t^*_{Pahala \to NW} = t^*_{Pahala \to ACO} - t^*_{NW \to ACO}$$

Solving for Q over the path, we derive $Q_{Pahala \to NW}$ from measured values at Pāhala and NW and at common frequencies, by solving (7).

$$\frac{\Delta t_{Pahala \to ACO} - \Delta t_{NW \to ACO}}{Q_{Pahala \to NW}} = \frac{\Delta t_{Pahala \to ACO}}{Q_{Pahala \to ACO}} - \frac{\Delta t_{NW \to ACO}}{Q_{NW \to ACO}} \qquad (7)$$

This procedure to estimate t^* works well when the successive Q_i differ by more than the “noise” in the Q–f trend. If the Q does not change more than the background fluctuations between successive segments, then the derived Q will have *non-Q-like* behavior due to the spectral noise, i.e., negative Q or extreme values. These fluctuations were hypothesized as due to seismic scattering variation (Butler 2020). In these instances, we may assume that the mean Q of the two segments is representative (see *Path Q segmentation*, Appendix A).

I derive the Q_{eff} for the azimuthal paths from earthquake to ACO, and use the relationship (*time/Q*) between propagation time and Q in order to subdivide the Q_{eff} among path segments (Butler, 2020). However, herein the segments are between earthquakes along the azimuthal path, whereas in Butler (2020) I used derived Q_{eff} segments between seismic stations along azimuth. Q_P and Q_S are measured and converted to their component moduli, bulk (Q_K) and shear (Q_S) attenuation.

Parenthetically, $Q_{Pahala \rightarrow NW} \equiv Q_{NW \rightarrow Pahala}$ due to the reciprocity of the seismic source and receiver for the anelastic Earth, e.g., $G(x, x'; t) = G^T(x', x; t)$ where G is the seismic Green tensor (Dahlen and Tromp, 1998).

4 Q TRANSECTS

4.1 Mauna Loa

I present the Q_K and Q_S measurements from the spectral analysis of the earthquake data along a transect beneath and through Mauna Loa. The raw data all have propagated to ACO, north of O‘ahu (Figure 1). I use the mechanics of t^* (*time*/Q) to separate the propagation into piecewise segments for path Q between earthquake sources and to ACO. In general, the Q values are frequency dependent, and linear in many cases. Because the mechanisms from which attenuation arises operate on the complex moduli μ and K, and to limit redundant information in the already complicated figures, Q_P is not plotted.

The Mauna Loa transect shown in Figure 3 [D] extends from Pāhala and Kama‘ehuakanaloa (deep and shallow events) to Mauna Loa NW (propagating near the crust/moho interface). The distance of the transect to Mauna Loa NW ranges from 70 km (Pāhala) and 116 km (Kama‘ehuakanaloa). Given the multiple earthquake magnitudes and depths in the Pāhala and Kama‘ehuakanaloa source regions, the distribution of Q_K values is relatively compact (Figure 3, [A]). Note significantly that *Q's* between the deep earthquakes (Pāhala and Kama‘ehuakanaloa) and NW show very similar *Q(f)* spectra in Figure 3 [A, C]. In Figure A5, only the deep transects are shown. The close overlap of the Pāhala and Kama‘ehuakanaloa paths in Figures 3 [D] and A5 gives credence to the close overlap of observed *Q(f),* though it remains surprising that paths differing by 46 km can be similar at high frequencies (~35 Hz). Butler (2020) considered possible scattering losses in the context of intrinsic Q

$$\frac{1}{Q_{eff}} = \frac{1}{Q_{intrinsic}} + \frac{1}{Q_{scattering}} \quad (8)$$

and postulated that the scattering effects are manifested in the high-frequency variability (scatter) in Q_{eff}, modifying the frequency trend for $Q_{intrinsic}$. From this perspective, the background scatter is surprisingly consistent.

At low frequency < 5Hz the $Q_K \sim 25$ for the five trends in Figures 3. Overall, the Q_K trend between Pāhala* (shallow earthquake nearest to the Pāhala deep swarm, Figures 1 [Right] and Figure 3[B]) and NW shows the highest attenuation—even when comparing with the Kamaʻehuakanaloa to NW paths. The broadest frequency range and highest Q_K characterizes the Pāhala deep to NW trend Figure 3[A]. Both Kamaʻehuakanaloa and Pāhala suggest that the bulk attenuation environment beneath the Mauna Loa edifice shares many common features.

For Q_S, the situation in Figure 3 [B] is very different, where much greater attenuation is seen for Pāhala*–NW than either Kamaʻehuakanaloa$_s$–NW or Pāhala$_s$–NW. For the deep Q_S trends in Figure 3 [C], the attenuation for both paths overlay and increase rapidly with frequency to Q_S in the thousands above 10 Hz. The commonality of the Q_K for both deep and shallow events is in strong contrast to Q_S. This dichotomy indicates that the physical mechanisms of attenuation for Q_K and Q_S differ.

4.2 The Summit and Both Sides of Mauna Loa

In the prior section the Mauna Loa transect integrated the total attenuation accrued in propagating beneath a traverse of Mauna Loa. Here, I subdivide the path into three sections:

Southeastern (Pāhala* and Kama‘ehuakanaloa to Summit), Northwestern (Summit to NW Mauna Loa), and the Summit. The time in propagating each segment is simplified to the distance divided by the group velocity of *P* and *S* wave first arrivals, observed at ACO. The primary shallow pathways occur near the moho— shared by Pāhala*, Kama‘ehuakanaloa, NW, and NW Caldera propagation (see Figure 1 [Right]). Table A2 shows earthquake source depths and *P*- and *S*-wave group velocities—where values are averaged for multiple events at a site. The Summit serves as a section encompassing both Mauna Loa caldera and NW of the Caldera with a 9 km radius. The Q_K and Q_S for these segments are plotted in the Figure 4. The Q values observed (Q_K ~9 and Q_S ~10) are significantly smaller than reported elsewhere.

From a Pacific transect near Wake Island, Butler et al., (1987) found Q_K near 200 at 2.5 Hz. At the periods of radial free oscillation modes (>>1 s), Durek and Ekström (1995) proposed an earth model with bulk attenuation limited to the aesthenosphere with Q_K ~ 175. For comparison with Kīlauea 2018 data, the path from the Halema‘uma‘u caldera is 46 km to the POHA seismic station at the Mauna Loa – Mauna Kea saddle, where the Q values near 1 Hz obtained by Butler (2020) are Q_K ~ 58 and Q_S ~ 81. For the Lau basin, Wei and Wiens (2020) report minimum Q values of Q_K ~21 and Q_S ~27 measured near 1 Hz, confined to the region immediately beneath the Lau back-arc spreading centers west of the Tonga Arc, noting that locations are not well resolved on a length and depth scale of <50 km..

Propagation at the Mauna Loa Summit from the southeast and toward the northwest manifest asymmetric Q_K and Q_S (Figure 5). The Q_K values to the northwest are much smaller than exhibited from the southeast. A conjecture on the cause of this asymmetry between the southeast and northwest is that trailing residual heat remains significant near the moho from the southeast apparent motion of the Hawai‘i hotspot southeast relative to the Pacific plate moving northwest (e.g., Wright and Klein, 2005). Partial melt and bulk attenuation will be discussed in section 5.3 Q_K and Partial Melt.

For shear attenuation—discussed in the following section—the northwest path is intermediate between low Q_S (larger shear attenuation) from Pāhala and higher Q_S from the Kama‘ehuakanaloa to the Summit path.

4.3 Kama‘ehuakanaloa and Pāhala Transect

The pathway transiting from Kama‘ehuakanaloa to Pāhala presents the only deep earthquakes in this study, and offers a view of Q_K and Q_S for both shallow (<12 km) and deep (>30 km) propagation. In Figure 6 the ubiquitous observation of $Q_K < Q_S$ holds true for the southeastern coast of Mauna Loa to the nascent Kama‘ehuakanaloa volcano. For shallow propagation, the Kama‘ehuakanaloa–Pāhala* path has a relatively high Q_S, which may underwrite the higher Q_S of the Kama‘ehuakanaloa–Summit transect, as seen in Figure 5. Given the influence of the higher Q_S offshore, in adjudicating the asymmetry of Mauna Loa Q the Pāhala*–Summit path is the preferred comparison for Summit–NW where $f < 11$ Hz, and the two paths are relatively symmetric. For $f > 11$ Hz the Summit–NW path shows higher Q_S and lower attendant attenuation. For the deep propagation (Figure 6) between Kama‘ehuakanaloa and Pāhala, the difference between Q_S and Q_K expands significantly. For Q_S the deep path has lower attenuation and the Q_K larger attenuation than the shallow case.

4.4 Transect maps of *Q*

The $Q(f)$ plots from Figures 2–6 are summarized in Figures 7 (Q_K) and 8 (Q_S), where the Q’s are plotted as a function of frequency (f) and Q within the narrow study region. The detail plots for Q_K and Q_S are shown together in Figure A6, for ease in comparison. The Figures 7 and 8 also show a color mapping of Q_K and Q_S in plan view, each independently grouped into five successive color bins by *Q factor*—note that the bins assigned by color differ between Q_K and Q_S. By color the *Q's* are ordered—blue > green > yellow > orange > red—from highest to lowest *Q*. The lowest *Q*'s (largest attenuation) are found in the Mauna Loa summit region, followed by the northwestern and southeastern slopes; the highest *Q's* (lowest attenuation) occur between the Northwest (NW) and ACO. The *Q* color-values are plotted as ellipses along the azimuth to ACO, where the overlapping paths to Kamaʻehuakanaloa are widened for clarity.

Although the detailed features of the seismic wave propagation cannot be resolved, the *P*-wave group velocities are in the range 7.3 to 7.7 km/s for shallow Pāhala and Kamaʻehuakanaloa events, respectively, and 7.9 km/s in common for deep events (see Table A2). These group velocities extend from the earthquake hypocenter to the Aloha Cabled Observatory location at 4.7 km below sea level. The depth to moho beneath Mauna Loa Summit is estimated as between ~18.5–16 km (Zucca, et al., 1982; Hill and Zucca, 1987; Park et al., 2009) In a tomographic inversion, Lin et al. (2014) find that the Mauna Loa Caldera and Pāhala events both estimate the base of crust at ~17 km, with a velocity of ~7.5 km/s. MacGregor et al., (2023) find a velocity of ~7.5 km/s at the base of a ~17 km thick crust beneath the Mākukona–Kahala saddle at the northwest coast of Hawaiʻi, where the moho velocity ~8–8.2 km/s. Given that the P-wave group velocities are comparable with the near-moho (e.g., peridotite) and lower oceanic crust (e.g., gabbro) values, propagation near the moho–crustal boundary is a reasonable assumption, except near ACO where upper crustal (basalt) propagation may also contribute.

To place this propagation into perspective, published estimates of the magma reservoir beneath Mauna Loa summit include: 3–9 km (Koyanagi, 1987); 3–5 km (Walter and Amelung, F., 2006); and 4.7 ± 1.1 km (Amelung et al., 2007). Hence the observed Q_K and Q_S. are measured and occur below the depth of estimates for the magma chamber.

In viewing the variation of Q_K along the azimuthal corridor to ACO, the greatest contrast in Q is found at earthquake site NW—which demarcates the boundary between segments ‘***b***’ and ‘***d***’. Between 6 and 14 Hz the smallest (largest attenuation) Q_K (~10–25) adjoins the highest Q_K (~100–2000), see Figures 7 and A6. For $\boldsymbol{Q_S}$ the situation is similar with the highest Q_K (~1000–3000). The boundaries are necessarily indistinct since the site is an earthquake hypocenter. I therefore conclude that there is a smooth transition across the 28 km distance (~17 wavelengths for *Vp*) between NW and NW Caldera from low to high attenuation, respectively.

5 ATTENUATION MECHANISMS

5.1 $\boldsymbol{Q_S(f)}$ and Activation Energy of Olivine

In Butler (2020) the activation energy, E^*, derived for basalt is 50 kJ/mol from T, P, and Q measured at two Hawai‘i scientific drilling sites. This 50 kJ/mol activation energy for basalt, derived from field data, is comparable to an experimentally determined value of 68 kJ/mol for basalt (Fontaine et al., 2005). Here I use experimentally determined olivine E^* as representative of an olivine subcrustal lithosphere. By employing experimental E^* and the thermal and pressure differences at two depths, the behavior of Q_S with earthquake depth can be compared with the observed Q_S variation.

For a frequency dependent activation process at Kama‘ehuakanaloa:

$$Q_S(f, T_1, P_1) = Q_0(f) exp \frac{E^* + \bar{V} P_1}{R T_1} \quad (9)$$

where E^* is an activation energy, f is frequency, R is the gas constant (8.314 J mole^{-1} °K^{-1}), $\bar{V}$ is molar volume (44×10^{-6} m^3 mole^{-1}). P_1 and P_2 are measured for Kama‘ehuakanaloa earthquake depths of 46 km and 11 km depths, respectively, from PREM (without ocean) (Dziewonski and Anderson, 1981) at 1.37×10^{9} and 2.8×10^{8} Nm^{-2}. T_1 (1620°) and T_2 (1490°) are temperatures (°*K*) derived from a Hawaiian Hotspot geotherm (Lee et al., 2009).

The propagation paths from the Kama‘ehuakanaloa earthquakes to ACO are nearly identical, and differ the most between the earthquake hypocenters. Faul and Jackson (2015) find that an olivine activation energy of 360 kJ/mol is broadly consistent with experimentally measured activation energies: Mg grain boundary diffusion (360 kJ/mol; Farver & Yund, 2000), diffusion creep (375 kJ/mol; Hirth & Kohlstedt, 2003), grainsize-sensitive viscoelastic relaxation (360 kJ/mol; Jackson & Faul, 2010), and dislocation recovery in fine-grained polycrystalline olivine, both synthetic and *San Carlos*, respectively (240±43, 355±81 kJ/mol; Farla et al., 2011).

The range of olivine activation energies (360–375 kJ/mol) provides a reasonable match to $Q_S(f)$ between 8 and 15 Hz at Kama‘ehuakanaloa (Figure 9 [Left]) between the deep and two shallow events, employing only a geotherm and pressure as a function of depth.

The second comparison (Figure 9 [Right]) shows estimates of a shear activation E^* between 240 and 260 kJ/Mol, congruent with Farla et al., (2011) experimental results on synthetic polycrystalline olivine, which aligns the Pāhala deep data with the shallow Pāhala earthquake between f = 2 and ~20 Hz. This is relatively consistent with the frequency range observed in (Figure 9 [Left]). Above 20 Hz, the deep Q_S data trends shallower at high frequencies. Both deep Q_S datasets in Figure 9 trend toward Q_S ~3500–4000 (very low attenuation).

We cannot definitively distinguish which E^* (singly or in concert with other olivine processes) is the primary olivine Q_S physical mechanism beneath Kama‘ehuakanaloa or Pāhala. Nonetheless, a reasonable case is made in linking laboratory-determined olivine activation energy to a real-world, activated attenuation process based solely on temperature and pressure changes and measured Q_S.

5.2 Q_K and Vesicular Basalt

Bulk attenuation can arise from the mismatch in bulk medium properties (Budiansky & O'Connell 1980)—incompressibility K, coefficient of volumetric thermal expansion α_V, thermal conductivity κ, and thermal diffusivity α_D. The observation of Q_K measured on the propagation path from Kahalui Maui to ACO (Butler, 2020) led to a hypothesis that water-filled vesicles within the crustal basalt provides a mechanism for bulk attenuation in the crust of the oceanic lithosphere. Butler (2020) notes that at widely differing drilling sites and sea floor ages within the Pacific, vesicular basalts are evident in the upper crust, with porosity values comparable to those observed within the Island of Hawai‘i. In Figure 10 I have plotted the Q_K from Butler et al. (1987) and Butler (2020), which show similar attenuation trends— from Q_K ~ 100 at 2 Hz to ~600 at 10 Hz. Including Q_K from Northwest Mauna Loa to ACO, somewhat larger attenuation is indicated, with Q_K ~100 at 4 Hz to ~ 500 at 10 Hz. Butler et al. (1987) found significant Q_K measured on a linear ocean bottom hydrophone array near Wake Island, and considered contributions from both heterogeneous materials and partial melting. Bulk attenuation is significant in the Alaskan subduction zone (Stachnik, et al., 2004), which is consistent with a vesicular basalt origin in the crust within the subducting plate.

Following Butler et al (1987), when does Q_K imply vesicular bulk attenuation, and when does partial melt bulk attenuation arise? For propagation near Wake Island the minimum age of the seafloor is 85 MA (Hilde et al., 1976), which is without overt volcanism. The Q_K in the segment from Kahului, Maui to ACO (Butler 2020) does not overlap obvious active volcanism (Haleakalā is 24 km orthogonal to the ACO path). While there is no apparent partial melt associated with Moloka‘i, the possibility cannot be eliminated. Between Kīlauea and ACO the mean *P*-wave group velocity observed was 7.1 km/s. As noted earlier velocities measured at ACO are in the range 7.3 to 7.7 km/s for shallow Pāhala and Kama‘ehuakanaloa earthquakes. These group velocities are proxies for the structure of along path, and indicate that propagation includes both the basaltic upper crust and gabbroic lower crust. Since gabbro has a lower porosity than vesicular basalt, whenever Q_K–f is observed in the oceanic crust, the contribution of the upper crust will predominate. Further development of a quantitative, vesicular basalt model for Q_K would enhance the interpretation of crustal-mantle, wave propagation and attenuation data.

5.3 Q_K and Partial Melt

Spetzler and Anderson (1968) suggested that a sharp dip in Q will be associated with the onset of partial melting in the mantle. Schmeling (1985) references a number of theoretical investigations focusing on the relationship between the seismic properties and partial melt, assuming different idealized melt geometries (Walsh, 1969; O’Connell and Budiansky, 1977; Mavko and Nur, 1975; Mavko, 1980), and modeled melts that can be assumed to occur in the form of tubes, films, and triaxial ellipsoidal inclusions of arbitrary aspect ratio. One conclusion of Schmeling (1985) is that triaxial ellipsoidal inclusions can be approximated by spheroidal inclusions. Hammond and Humphries (2000) modeled "Melt squirt," a term coined by Mavko and Nur (1975)— relaxation occurring when pressure differences between neighboring inclusions drive fluid flow—wherein the melt is a network of realistically shaped conduits joining ellipsoidal pores. Hammond and Humphries (2000) conclude, “We argue below that these pressure differences probably do not drive enough melt squirt to provide significant relaxation. Thus, bulk attenuation due to melt squirt is most likely not important in the seismic band." Wei and Wiens (2020) note that there is no well-characterized physical mechanism for bulk attenuation in the mantle (Faul & Jackson, 2015), and referred to Li and Weidner (2013), who suggested that "when seismic waves travel though a partially molten region, the stress perturbation will change melt fraction through a solid-liquid phase change and thus cause bulk attenuation."

Lyakhovsky et al. (2021) presents a thermodynamic equilibrium, partial-melt framework for bulk attenuation, quoting from their paper:

- "The suggested mechanism considers solid-melt phase transition at thermodynamic equilibrium. Any pressure change, that takes the system out of thermodynamic equilibrium, causes solidification or melting which modifies the heat balance according to the Clausius-Clapeyron equation. The latent heat (sink or source) is transferred away or towards the interface by conductive-advective mechanism, heating or cooling the entire rock mass, and leading to energy loss and dissipation of the mechanical energy and to seismic wave attenuation."
- "Mathematical formulation of this moving boundary or Stefan problem includes heat, mass, and force balance equations."
- "The analytical solution for the heat balance equation, including latent heat associated with the motion of the solid-melt interface, as well as temperature variations of the melt inclusion, provides the relation between pressure and volumetric strain oscillations."
- "Wave attenuation, or quality factor (Q) is calculated from the time delay between pressure and strain oscillations, or the ratio between real and imaginary bulk moduli."

This partial melt model of Lyakhovsky et al. (2021) is presented in Figure 11, where the Q_K–frequency data for the varied pathways of this study are plotted. The quality of the fits of the data to the model is encouraging, and provides for a basis for interpreting cell size and melt fraction in the context of measured attenuation versus frequency. The highest Q_K trend (“d” in red) in Figure 11 is measured from 37 km northwest of the Caldera to ACO, whereas the other paths interact with the Mauna Loa Summit, Pāhala and Kama‘ehuakanaloa closest to proximal volcanism. Given concordance of the observed Q_K–f trends with the Q_K–f model of partial melt, the model meets the usefulness criteria within the constraints of the model space.

6 ATTENUATION AND SEISMICITY

In the prior sections I have reviewed attenuation mechanisms which may underlie the observed Q_K and Q_S variation along the azimuthal corridor connecting ACO, Mauna Loa, Pāhala, and Kama‘ehuakanaloa. The Q_K and Q_S mechanisms are very different, and Q_K and its concomitant higher attenuation is considered now. Attenuation effects are evident for the broad physiographic features of the volcano—minimum Q (maximum attenuation) as seen beneath the Mauna Loa Caldera and Summit is not a surprise. Searching for additional correspondence between variation in Q_K with other parameters of geophysical significance, seismicity stands paramount. Since each earthquake hypocenter radiates seismic waves which are affected by the local and path attenuation, the observation of seismicity at some locality but not at another, potentially may present a causative connection. Recently, Matoz et al. (2020) relocated all Hawai‘i Island earthquakes between 1986 and 2018. The paper refocuses into sharp clarity prior indistinct features. Figure 12 plots the Q_K map from Figure 7, for comparison with the Matoza et al. (2020) relocated seismicity.

I restrict our comparison to the regional overlap of the Q_K map in Figure 7 with the high-seismicity, rectangular **C** region designated by Matoza et al. (2020). At the far right, depth cross-sections for the **C** region, both length-wise and width-wise (**C′**), are presented. Most significantly, there is a clear demarcation between shallow (<15 km in red) and deep (>30 km in blue) earthquakes where there is a paucity of hypocenters compared with the adjoining the shallow and deep events from this study.

In Figure 3[D] the propagation paths of deep earthquakes in Pāhala and Kamaʻehuakanaloa cross this 15–30 km seismic gap. The Q_K range of ~40–200 (low to high frequency) for segment K_d–P_d (c) is significant (Figure 3[A] and A5 deep transect). By the partial-melt model of bulk attenuation (Figure 11), the mechanism is consistent with 5.0 mm cell size and a melt fraction of ~ 0.3%.

The Matoza et al. (2020) study relocated defined earthquake events. In contrast, Wilding et al. (2023) “leverage advances in earthquake monitoring with deep learning algorithms to image structures underlying…” a swarm of earthquakes near Pāhala at 30–40 km depth, using the continuous data streams from the Earthscope Data Management Center. The study extended from November 2018 through April 2022—fifteen of these deep events with M_L >3.9 contributed to the present study. Wilding et al. (2023) find a “complex of mantle sills” near Pāhala at 36–46 km depth—termed the Pāhala sill complex (PSC). Their transect from Mauna Loa to Pāhala closely follows the azimuthal corridor to ACO. The hypocenter window of low seismicity discussed between 15 and 30 km is considered by Wilding et al. (2023) to be the “Pāhala–Mauna Loa seismicity band” … “consistent with proposed magma transport between PSC and the Mauna Loa edifice (Wright and Klein, 2006).”

Wilding et al. (2023) point out that, “Imaging the magma plumbing systems from the mantle to crust remains challenging for most geophysical methods such as seismic tomography, geodetic inversion, and gravity and electromagnetic surveys, because these methods typically are unable to resolve the distribution and transportation of magma (Magee et al., 2018).” Perhaps the most compelling evidence to date is observation of LP earthquakes, which are sources of harmonic tremor linked with magma flow (Julian, 1994; Chouet, 1996). “Harmonic tremor is the seismic indicator of magma movement and volcanic eruptions in Hawai‘i.” (Koyanagi, 1987) . However, Aki, K. and Koyanagi (1981) also conjectured, “it may be that most channels transport magma aseismically, and only those with strong barriers generate tremor.”

Bulk attenuation presents a new tool for assessing the existence of partial melt at depth, wherever there is contact at the solidus between magma and solid. Bulk attenuation dominates with $Q_K < Q_S$ throughout the Mauna Loa – Pāhala – Kama‘ehuakanaloa systems. In addition to partial melt effects, bulk attenuation is also hypothesized from water-saturated vesicular basalts in the shallow oceanic crust (Butler 2020). Neither of the bulk mechanisms are activated processes, in contrast to shear attenuation, which fits an activation energy process between ~2 and ~20 Hz. Whenever Q_K is measured beneath the shallow oceanic crust, a *prima facie* case is made for partial melt as the causative origin. These Q_K factors indicate maximum bulk attenuation and partial melt lies beneath the Mauna Loa Summit near the moho. To the northwest and southeast of the Summit, the bulk attenuation—and hence partial melt—varies. The apparent 100 km length of the Mauna Loa partial melt corridor near the moho begins beneath the northwest slope of Mauna Loa, approximately midway between NW and the Summit, and continues beneath the Caldera through to Kama‘ehuakanaloa.

7 DISCUSSION

This study was initiated to understand the nature of high frequency (>50 Hz) wave propagation from Mauna Loa earthquakes propagating to the Aloha Cabled Observatory (ACO), following the study of 2018 Kīlauea swarm. As I delved further in the shallow (<12 km) and deep (>30 km) earthquakes and their paths, the study morphed significantly into an analysis of attenuation along the narrow (1°) azimuthal propagation corridor to ACO from Mauna Loa–Pāhala–Kamaʻehuakanaloa. In this study I focused only on Q_K (bulk) and Q_S (shear) attenuation factors dependent upon the complex elastic moduli (K incompressibility and μ rigidity). Here Qp was treated as a means to derive Q_K.

The effective Q_K and $\boldsymbol{Q_S}$ for Mauna Loa paths to ACO are both lower (more attenuating) than Kīlauea and manifest a similar linear trend with frequency. For all paths, $Q_K < \boldsymbol{Q_S}$ indicating that bulk attenuation dominates shear. $\boldsymbol{Q_S}$ from deep events in Pāhala and Kamaʻehuakanaloa show similar frequency trajectories: $dQ_S/df \sim 200$ from 2–15 Hz, then both change course to $Q_S/df \sim 30$ from 15–50 Hz, suggesting a change in the underlying attenuation mechanism. The Pāhala deep Q_K also follow a trajectory $Q_K/df \sim 30$ (offset from $\boldsymbol{Q_S}$ by a Q factor of ~2500), though it is not obvious why, given the different underlying attenuation mechanisms.

Given the diversity of path $Q(f)$ propagating to ACO, the paths were separated into segments derived from time/Q sections. For example the path Pāhala–ACO is converted to a Pāhala–NW segment, and similarly for paths from Kamaʻehuakanaloa, Mauna Loa Caldera, and Summit. Thus, a Q transect of Mauna Loa from southeast to northwest is derived. For Q_K the $Q_K(f)$ trends are linear, and similar for both deep and shallow paths, whereas the deep Q_S paths have much lower attenuation than their shallow counterparts. The Mauna Loa Summit shows the largest attenuations in the study with Q_K and $\boldsymbol{Q_S}$ ~10. By comparing the Q factors from the southeast to the Summit and from the Summit to the northwest, Q_K is smaller (more attenuating) on the northwest slope than the southeast slope which may indicate residual heat from the hotspot apparent motion southeast relative to the Pacific plate moving northwest. For paths between Pāhala an'd Kama‘ehuakanaloa, the deep events show lower Q_K and higher QS, with shallow events intermediate. The overall propagation to ACO is close to the moho, as constrained by *P*- and *S*-wave group velocities. To place the derived Q and their segment boundaries into perspective, Q_K and $\boldsymbol{Q_S}$ maps are made showing the distribution of paths in a hierarchy sorted by Q factors.

Having measured and derived $\boldsymbol{Q_S}$ and Q_K along the narrow corridor, focus turned toward understanding the underlying attenuation mechanisms. Using a hotspot geotherm, pressure from the PREM earth model, and experimental activation energies for olivine, I was able to project the $\boldsymbol{Q_S}$ from two Kama‘ehuakanaloa shallow earthquakes to the observed $\boldsymbol{Q_S}$ for the deep earthquake, and similarly for Pāhala shallow and deep earthquakes. Hence, experimentally derived olivine activation energies are successfully matched with field measurements at Pāhala and Kama‘ehuakanaloa. For the deep earthquakes, there are observed changes in Q–f trends at higher frequency, which likely indicate changes in the activated attenuation mechanism. However, for shallow earthquakes **the** $\boldsymbol{Q_S}$ data at higher frequency data for shallow paths do not meet SNR criterion, thus affording no comparison or estimation of E^*.

Comparing Q_K measured from paths near Wake Island, Kīlauea (Maui–ACO), and now Mauna Loa (NW–ACO), model constraints are suggested for shallow crustal propagation where Q_K arises from the heterogeneity of water-filled, vesicular basalts. The range of Q_K observed is

~100–600. This assessment is qualitative, and a quantitative model including wave propagation effects would enhance further understanding of this attenuation process.

To understand Q_K where propagation is near the moho—where gabbros and olivine do not show sufficient bulk heterogeneity—the primary mechanism of Q_K is conjectured as due to partial melting. This makes eminent sense in the volcano–hotspot region of the study. I have applied a thermodynamic equilibrium model to the Q_K data set, and found excellent fits. This model projects Q_K and f from a per-cent, partial melt fraction, and the size of the cell and its inclusion. By applying the partial-melt model to the mapped distribution of Q_K, the variation of the melt fraction and apparent cell size may be viewed along the transect to ACO. Finally, I have compared the Q_K with mapped seismicity and observe that areas of low seismicity may also have significantly low Q_K—hence consistent with a partial melt pathway for magma flow. This interpretation is consistent both with discussion in the reference literature, and with the most recently completed earthquake relocation efforts and machine learning analysis.

7.1 Culmination

I have measured extensive Q_K and Q_S along a transect through Hawai‘i from Kama‘ehuakanaloa volcano, a Pāhala deep swarm, and Mauna Loa to the Aloha Cabled Observatory. Generally, $Q_K < Q_S$, and both are lowest beneath the Mauna Loa Summit. Bulk and shear attenuation mechanisms have been explored and modeled. Q_K and Q_S differ substantially, underscoring their differing underlying mechanisms. Applying a thermodynamic equilibrium model of partial melt to $Q_K(f)$ data provides a reasonable qualitative and quantitative fit, which elevates $Q_K(f)$ as a remote sensor for partial melt.

Data and Resources

All earthquake locations (2011–2018) were obtained from the relocated catalog of Matoza et al. (2020), and thereafter (2019-2023) from the USGS Hawaiian Volcano Observatory network catalog (https://earthquake.usgs.gov/earthquakes/search/) The Matoza et al., (2020) catalog is now integrated into the HVO catalog. ALOHA hydrophone data were downloaded from the University of Hawai‘i Aloha Cabled Observatory (ACO).

Acknowledgements

I thank Don L. Anderson for his formative discussions of bulk attenuation. I thank the University of Hawai‘i and the NSF for supporting the Aloha Cabled Observatory.
HIGP contribution number 2494.

References

Aki, K. (1967). Scaling law of seismic spectrum, J. Geophys. Res. 72, no. 4, 1217–1231.

Aki, K. and Koyanagi, R., 1981. Deep volcanic tremor and magma ascent mechanism under Kilauea, Hawaii. *Journal of Geophysical Research: Solid Earth*, *86*(B8), pp.7095-7109.

Amelung, F., Yun, S.H., Walter, T.R., Segall, P. and Kim, S.W., 2007. Stress control of deep rift intrusion at Mauna Loa volcano, Hawaii. *Science*, *316*(5827), pp.1026-1030.

Anderson, D.L., 1989. *Theory of the Earth*. Blackwell Scientific Publications, p. 300.

Brune, J. N. (1970). Tectonic stress and the spectra of seismic shear waves from earthquakes, J. Geophys. Res. 75, no. 26, 4997–5009.

Budiansky, B. & O’Connell, R.J., 1980. Bulk dissipation in heterogeneous media, in *Solid Earth Geophysics and Geotechnology,* pp. 1–10, ed. Nasser, S. N., American Society of Mechanical Engineers.

Butler, R., C. S. McCreery, L. N. Frazer, and D. A. Walker (1987), High-frequency seismic attenuation of oceanic P- and S-waves in the western Pacific, *Journal of Geophysical Research Solid Earth,* **92**, 1383–1396 (1987).

Butler, R., 2018. High-frequency (>100 Hz) earthquakes North of Moloka‘i detected on the seafloor at the Aloha cabled observatory high-frequency earthquakes North of Moloka‘i detected on the seafloor, *Bull. seism. Soc. Am.,* **108**(5A), 2739–2747.

Butler, R., 2019. Composite earthquake source mechanism for 2018 M w 5.2–5.4 Swarm at K Kīlauea Caldera: antipodal source constraint, *Seismol. Res. Lett.,* **90**(2A), 633–641.

Butler, R., 2020. Bulk, shear and scattering attenuation beneath Hawaiian Volcanos and in the oceanic crust extending to the Aloha Cabled Observatory. *Geophysical Journal International*, *223*(1), pp.543-560.

Chouet, B.A., 1996 (Mar 28). Long-period volcano seismicity: its source and use in eruption forecasting. Nature 380, 309 – 316.

Cormier VF. The effect of attenuation on seismic body waves. Bulletin of the Seismological Society of America. 1982 Dec 1;72(6B):S169-200.

Dahlen, F. A. and Tromp, J., 1998. Theoretical global seismology. In Theoretical Global Seismology. Princeton university press, 1025 pp.

Durek, J.J. and Ekström, G., 1996. A radial model of anelasticity consistent with long-period surface-wave attenuation. *Bulletin of the Seismological Society of America*, *86*(1A), pp.144-158.

Dziewonski, A.M. & Anderson, D.L., 1981. Preliminary reference Earth model, *Phys. Earth planet. Inter.,* **25**(4), 297–356.

Farla, R.J.M., Kokkonen, H., Fitz Gerald, J.D., Barnhoorn, A., Faul, U.H. and Jackson, I., 2011. Dislocation recovery in fine-grained polycrystalline olivine. Physics and Chemistry of Minerals, 38(5), pp.363-377.

Farver JR, Yund RA. 2000. Silicon diffusion in forsterite aggregates: implications for diffusion accommodated creep. *Geophys. Res. Lett.* 27:2337–40

Faul, U. and Jackson, I., 2015. Transient creep and strain energy dissipation: An experimental perspective. Annual Review of Earth and Planetary Sciences, 43, pp.541-569.

Fontaine, F. R., Ildefonse, B., & Bagdassarov, N. (2005) Temperature dependence of shear wave attenuation in partially molten gabbronorite at seismic frequencies. Geophysical Journal International, 163: 1025-1038.

Hammond, W.C. and Humphreys, E.D., 2000. Upper mantle seismic wave attenuation: Effects of realistic partial melt distribution. *Journal of Geophysical Research: Solid Earth*, *105*(B5), pp.10987-10999.

Hansen, S., Thurber, C., Mandernach, M., Haslinger, F. & Doran, C., 2004. Seismic velocity and attenuation structure of the east rift zone and south flank of Kilauea Volcano, Hawaii, *Bull. seism. Soc. Am.,* **94**(4), 1430– 1440.

Hilde, T. W. C., N. Isezaki, and J. M. Wageman, 1976. Mesozoic sea-floor spreading in the north Pacific, in The Geophysics of the Pacific Ocean Basinand its Margins, Geophys.Monogr.Ser.vol. 19, edited by G. H. Sutton, M. H. Manghnani, and R. Moberly, pp. 205-226, AGU, Washington, D.C.

Hill, D. P., and J. J. Zucca (1987), Geophysical constraints on the structure of Kilauea and Mauna Loa volcanoes and some implications for seismomagmatic processes, *U.S. Geol. Surv. Prof. Pap.*, **1350**, 903–917.

Hirth G, Kohlstedt DL. 2003. Rheology of the upper mantle and the mantle wedge: a view from the experi- mentalists. Geophys. Monogr. 138:83–105.

Jackson, I. and Faul, U.H., 2010. Grainsize-sensitive viscoelastic relaxation in olivine: Towards a robust laboratory-based model for seismological application. Physics of the Earth and Planetary Interiors, 183(1-2), pp.151-163.

Julian, B.R., 1994. Volcanic tremor: nonlinear excitation by fluid flow. Journal of Geophysical Research 99 (B6), 11859 – 11877.

Kaneko, Y., and P. M. Shearer (2014). Seismic source spectra and estimated stress drop derived from cohesive-zone models of circular subshear rupture, Geophys. J. Int. 197, no. 2, 1002–1015.

Kaneko, Y., and P. M. Shearer (2015). Variability of seismic source spectra, estimated stress drop, and radiated energy, derived from cohesive-zone models of symmetrical and asymmetrical circular and elliptical ruptures, J. Geophys. Res. 120, no. 2, 1053–1079.

Koyanagi, R.Y., 1987. *Seismicity associated with volcanism in Hawaii: Application to the 1984 eruption of Mauna Loa volcano*. Open-File Report 87-277, Department of the Interior, US Geological Survey.

Lee, C.T.A., Luffi, P., Plank, T., Dalton, H. and Leeman, W.P., 2009. Constraints on the depths and temperatures of basaltic magma generation on Earth and other terrestrial planets using new thermobarometers for mafic magmas. Earth and Planetary Science Letters, 279(1-2), pp.20-33.

Li, L., & Weidner, D. J. (2013). Effect of dynamic melting on acoustic velocities in a partially molten peridotite. Physics of the Earth and Planetary Interiors, 222, 1–7. https://doi.org/10.1016/j.pepi.2013.06.009

Lin, G., Shearer, P.M., Matoza, R.S., Okubo, P.G. and Amelung, F., 2014. Three-dimensional seismic velocity structure of Mauna Loa and Kīlauea volcanoes in Hawaii from local seismic tomography. *Journal of Geophysical Research: Solid Earth*, *119*(5), pp.4377-4392.

Lin, G., Shearer, P.M., Amelung, F. & Okubo, P.G., 2015. Seismic tomography of compressional wave attenuation structure for Kīlauea Volcano, Hawaiʻi, *J. geophys. Res.,* **120,** 2510–2524.

Lyakhovsky, V., Shalev, E., Kurzon, I., Zhu, W., Montesi, L. and Shapiro, N.M., 2021. Effective seismic wave velocities and attenuation in partially molten rocks. *Earth and Planetary Science Letters*, *572*, p.117117.

MacGregor, B. G., R. A. Dunn, A. B. Watts, C. Xu, and D. J. Shillington (2023). A seismic tomography, gravity, and flexure study of the crust and upper mantle structure of the Hawaiian Ridge, Part 1, Journal of Geophysical Research: Solid Earth, https://doi.org/10.1029/2023JB027218

Madariaga, R. (1976). Dynamics of an expanding circular fault, Bull. Seis- mol. Soc. Am. 66, no. 3, 639–666.

Madariaga, R. (1977). High-frequency radiation from crack (stress drop) models of earthquake faulting, Geophys. J. Int. 51, no. 3, 625–651.

Magee, C., C. T. E. Stevenson, S. K. Ebmeier, D. Keir, J. O. S. Hammond, J. H. Gottsmann, K. A. Whaler, N. Schofield, C. A.-L. Jackson, M. S. Petronis, B. O'Driscoll, J. Morgan, A. Cruden, S. A. Vollgger, G. Dering, S. Micklethwaite, M. D. Jackson, Magma Plumbing Systems: A Geophysical Perspective. *J. Petrol.* 59, 1217–1251 (2018). doi:10.1093/petrology/egy064

Mavko. G.M., 1980. Velocity and attenuation in partially molten rocks. J. Geophys. Res., 85, 5173—5189.

Mavko, G.M. and Nur, A., 1975. Melt squirt in the asthenosphere. J. Geophys. Res., 80, 1444–1448.

Matoza, R.S., Okubo, P.G. and Shearer, P.M., 2021. Comprehensive High-Precision Relocation of Seismicity on the Island of Hawaiʻi 1986–2018. Earth and Space Science, 8(1), p.e2020EA001253.

Neal, C.A., *et al.*, 2019. The 2018 rift eruption and summit collapse of Kīlauea Volcano, *Science,* **363**(6425)367–374.

O'Connell, R.J. and Budiansky, B.. 1977. Viscoelastic properties of fluid-saturated cracked solids. J. Geophys. Res., 82, 571 9–5735.

Park, J., Lindberg, C.R. & Vernon, F.L., 1987. Multitaper spectral analysis of high-frequency seismograms, *J. geophys. Res.,* **92**(B12), 12 675–12 684.

Park, J., Morgan, J.K., Zelt, C.A. and Okubo, P.G., 2009. Volcano-tectonic implications of 3-D velocity structures derived from joint active and passive source tomography of the island of Hawaii. *Journal of Geophysical Research: Solid Earth*, *114*(B9).

Scherbaum, F. and Wyss, M., 1990. Distribution of attenuation in the Kaoiki, Hawaii, source volume estimated by inversion of P wave spectra. *Journal of Geophysical Research: Solid Earth*, *95*(B8), pp.12439-12448.

Schmeling, H., 1985. Numerical models on the influence of partial melt on elastic, anelastic and electric properties of rocks. Part I: elasticity and anelasticity. Phys. Earth Planet. Inter., 41: 34—57.

Shearer, P. M., G. A. Prieto, and E. Hauksson (2006). Comprehensive analy- sis of earthquake source spectra in southern California, J. Geophys. Res. 111, no. B6, doi: 10.1029/2005JB003979.

Spetzler, H. and D.L. Anderson, 1968. The Effect of Temperature and Partial Melting on Velocity and Attenuation in a Simple Binary System, JGR VoL. 73, No. 18.

Stachnik, J.C., Abers, G.A. and Christensen, D.H., 2004. Seismic attenuation and mantle wedge temperatures in the Alaska subduction zone. *Journal of Geophysical Research: Solid Earth*, *109*(B10).

Hanks, T.C. & Thatcher, W., 1972. A graphical representation of seismic source parameters, J. Geophys. Res., 77(23), 4393–4405.

Walsh, J.B., 1969. New analysis of attenuation in partially melted rock. .1. Geophys. Res.. 74, 4333–4337.

Walter, T.R. and Amelung, F., 2006. Volcano-earthquake interaction at Mauna Loa volcano, Hawaii. *Journal of Geophysical Research: Solid Earth*, *111*(B5).

Wei, S.S. and Wiens, D.A., 2020. High bulk and shear attenuation due to partial melt in the Tonga-Lau back-arc mantle. Journal of Geophysical Research: Solid Earth, 125(1), p.e2019JB017527.

Wilding JD, Zhu W, Ross ZE, Jackson JM. The magmatic web beneath Hawai ‘i. Science. 2023 Feb 3;379(6631):462-8.

Wright, T.L. and Klein, F.W., 2006. Deep magma transport at Kilauea volcano, Hawaii. *Lithos*, *87*(1-2), pp.50-79.

Zucca, J.J., Hill, D.P. and Kovach, R.L., 1982. Crustal structure of Mauna Loa volcano, Hawaii, from seismic refraction and gravity data. *Bulletin of the Seismological Society of America*, *72*(5), pp.1535-1550.

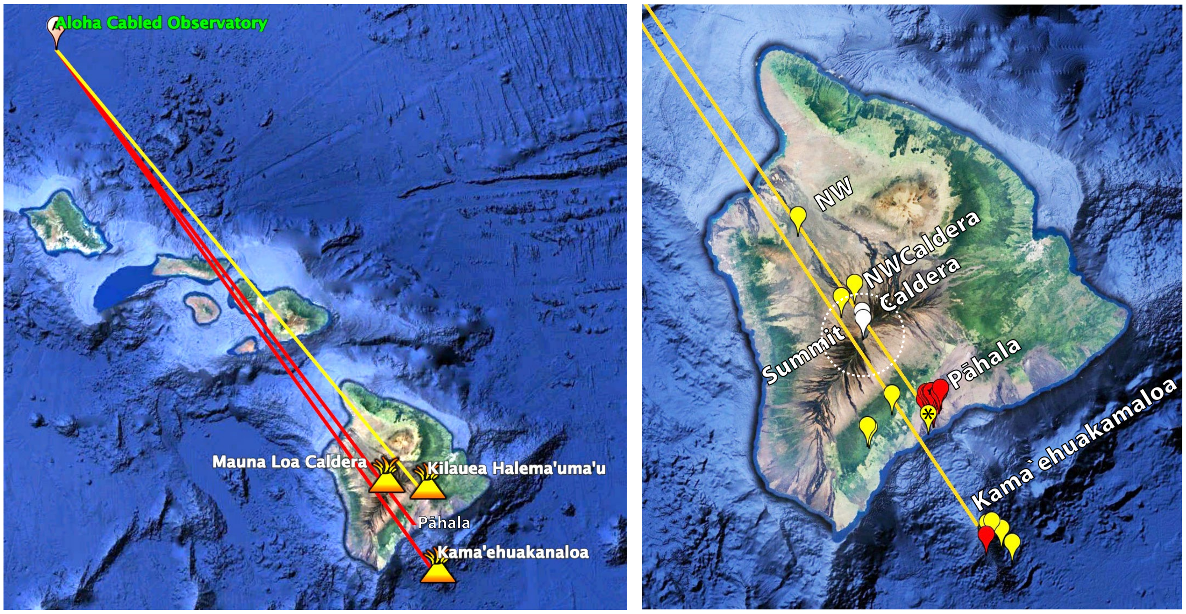

Figure 1. [Left] plots the key propagation paths of caldera earthquakes from Mauna Loa, Kama‘ehuakanaloa, and the deep seismicity near Pāhala; these paths to the Aloha Cabled Observatory (ACO) are shown in red, whereas the yellow path is from Kīlauea’s caldera (Butler 2020). The azimuths from ACO to Kama‘ehuakanaloa, and Pāhala differ by < 1°. The relatively close proximity of the paths between ACO and the northwest Hawai‘i Island advocate for common, parallel attenuation features. [Right] Map of Hawai‘i showing earthquake data locations. Pathways in yellow connect ACO with Pāhala, Kama‘ehuakanaloa, and Maunaloa. Shallow events with depths < 12 km are yellow, deep events > 30 km plotted red, and very shallow events within the Mauna Loa Caldera (~ -0.2 km) are in white. The Pāhala earthquake marked by * is the shallow event (yellow) closest to the Pāhala deep seismicity—the other three shallow Pāhala events are 12 to 22 km from the Pāhala deep swarm. The summit region includes two earthquakes northwest of Mauna Loa Caldera.

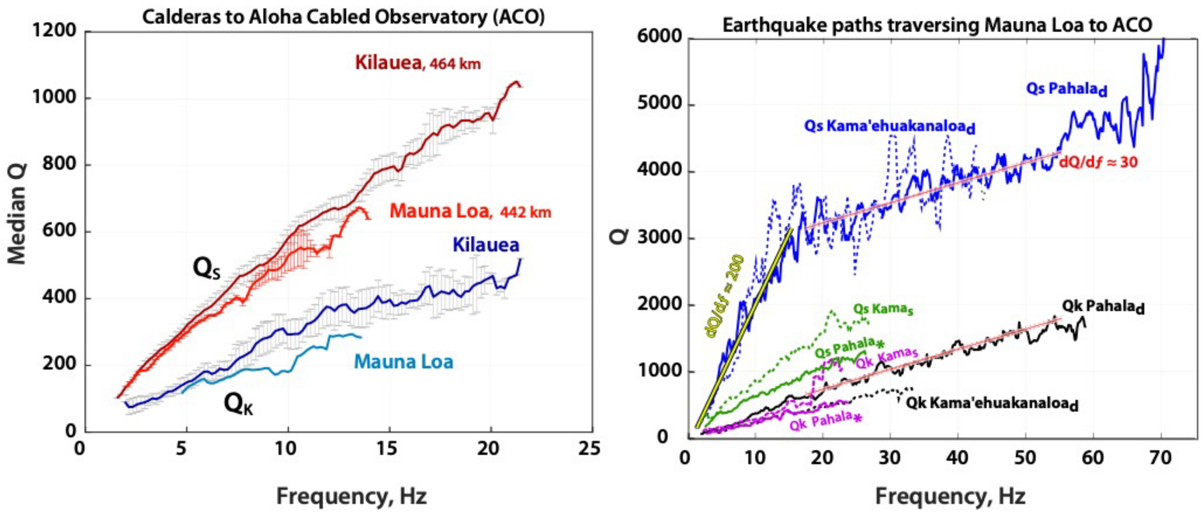

Figure 2. [Left] A direct comparison of the measured effective Q—bulk Q_K and shear Q_S—from Kīlauea and Mauna Loa Calderas, Halema‘uma‘u and Moku‘āweoweo, respectively. The earthquake hypocenters had median depths of about 0.3 km at Kīlauea and -0.2 km at Mauna Loa, and similar distances > 440 km to ACO. [Right] Each of the Q_K and Q_S paths start southeast of Mauna Loa and propagate beneath Mauna Loa to ACO. Solid lines refer to Pāhala, whereas a dotted line refers to Kama‘ehuakanaloa. Deep and shallow earthquake sites are designated with appended subscripts “d” or “s”, respectively, which include stacked data. The single Pāhala shallow earthquake closest to the deep seismicity is marked with a subscript *. Note the diversity of Q-trends arising within this crowded corridor.

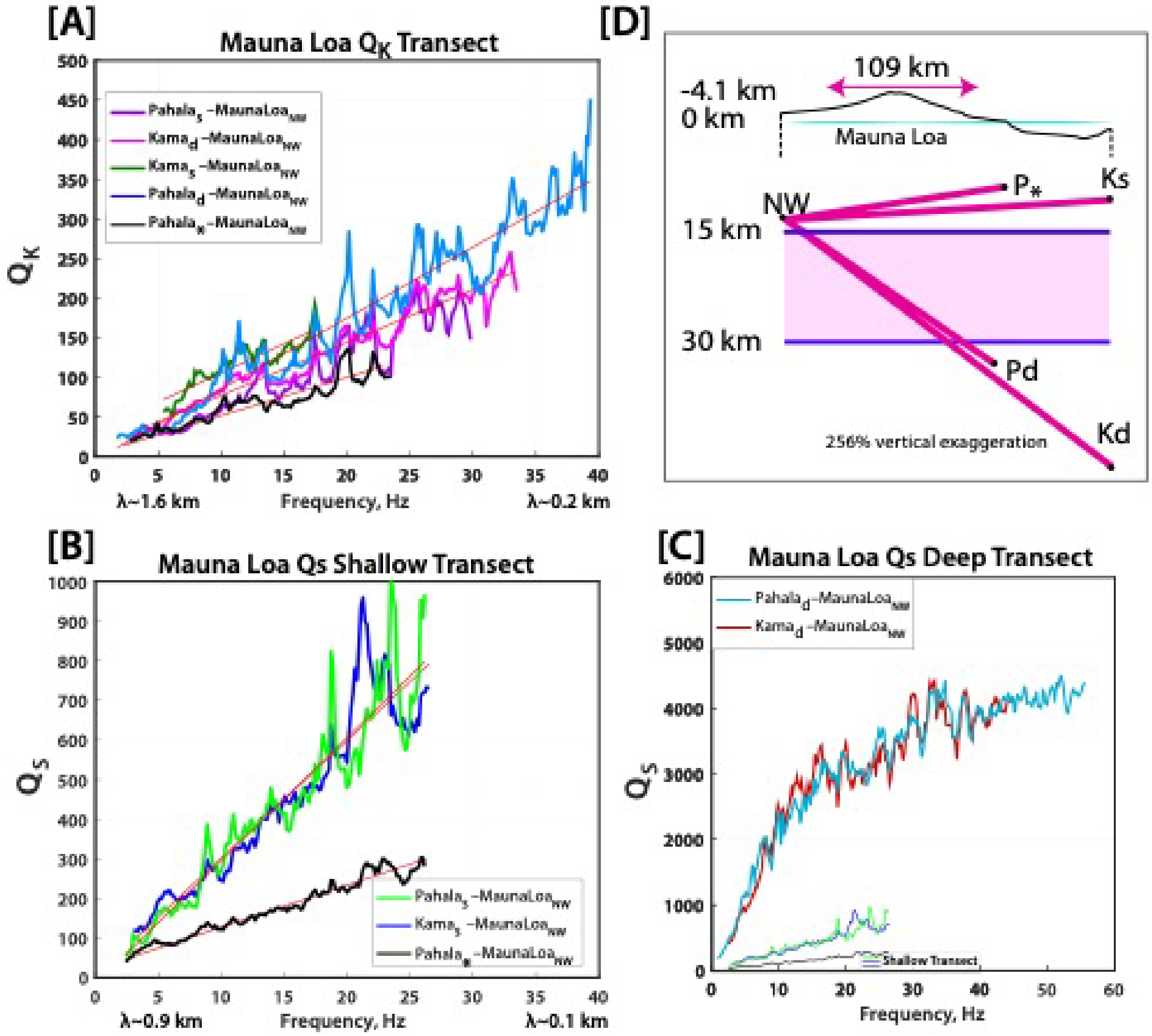

Figure 3. Several Mauna Loa transects [ABC] from southeast to northwest are shown for Q_K and Q_S. Paths follow the nomenclature of Figure 2. The earthquake at Mauna $\mathrm{Loa}_{\mathrm{NW}}$ is shallow at 13.3 km depth. Segments are named by their endpoints. The subfigure [A] is Q_K, and Q_S plots in subfigures [B, C] for shallow and deep, respectively. Representative seismic wavelengths are noted for low and high frequency—for Q_K the Vp wavelength is shown. Note the Q_K and Q_S linear frequency trends in the subfigures [A, B]. For the deep Q_S transect [C] there are one or more changes in slope, suggesting more than one shear wave attenuation mechanism is operating. The propagation paths beneath Mauna Loa are simply illustrated in the cartoon [D], where “P” implies Pāhala, “K” Kama‘ehuakanaloa, “s” shallow, “d” deep, and “*” indicates the Pāhala shallow earthquake closest to the Pāhala deep swarm (Figure 1 [Right]). Note the similarity across the frequency band between Mauna $\mathrm{Loa}_{\mathrm{NW}}$–$\mathrm{Pāhala}_{d}$ and Mauna $\mathrm{Loa}_{\mathrm{NW}}$–$\mathrm{Kama}_{d}$ transects within both [A] & [C], which share common structure propagating to NW [D]. See also Figure A5.

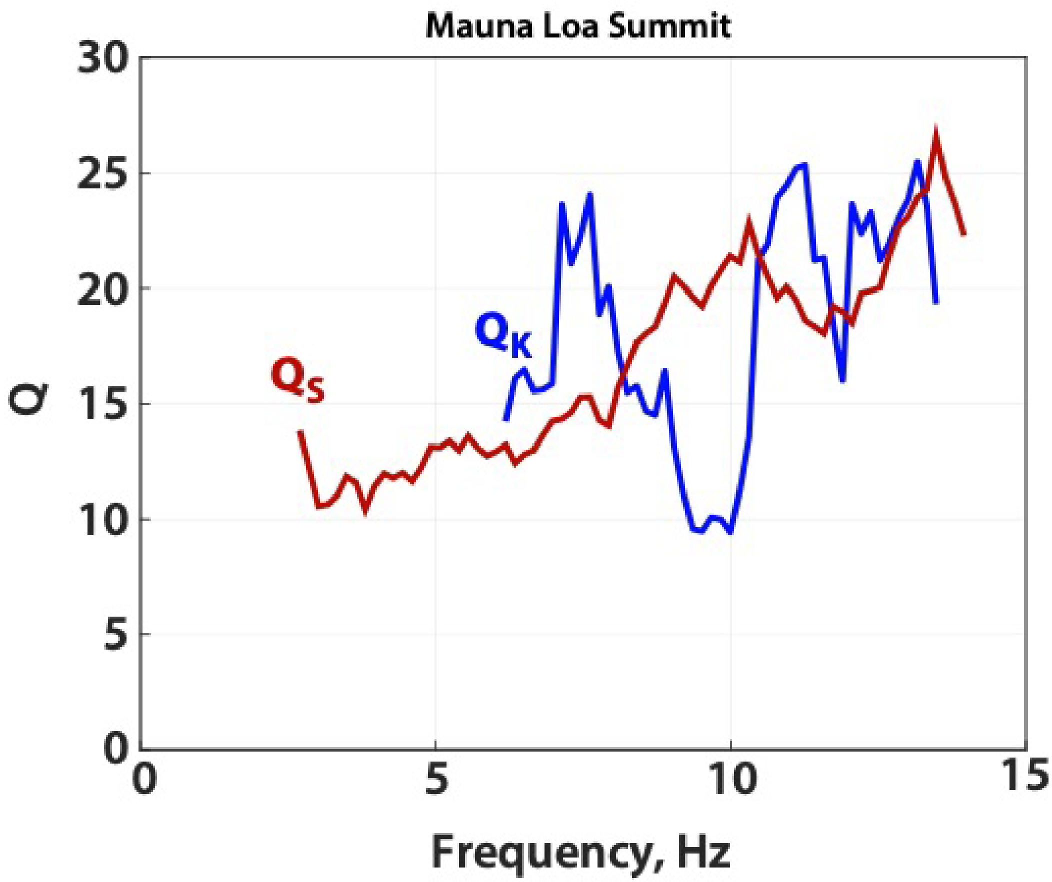

Figure 4. The bulk Q_K (blue) and shear Q_S (red) are plotted from the Mauna Loa Summit region, which encompasses depths from -0.2 to 10.7 km.

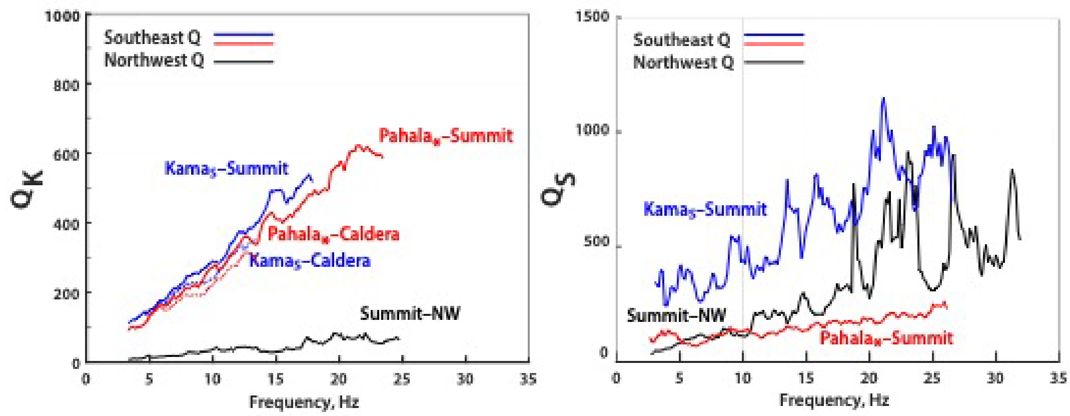

Figure 5. The Q_{eff} for segments from Pāhala and Kama‘ehuakanaloa to the Summit are plotted in red and blue, whereas pathways from Summit to NW Mauna Loa are shown in black. [Left] For Q_K northwest paths are much attenuated with respect to the southeastern paths from Pāhala and Kama‘ehuakanaloa. This presents evidence that more bulk attenuation at Mauna Loa takes place northwest of the Summit region than to the southeast. Nonetheless, the southeastern paths from Kama‘ehuakanaloa and Pāhala are very similar. [Right] For Q_S the Summit–NW path (black) lies between the Kama‘ehuakanaloa–Summit and Pāhala–Summit paths, overlapping the Kama‘ehuakanaloa trend at higher frequency, and Pāhala trend at lower frequency.

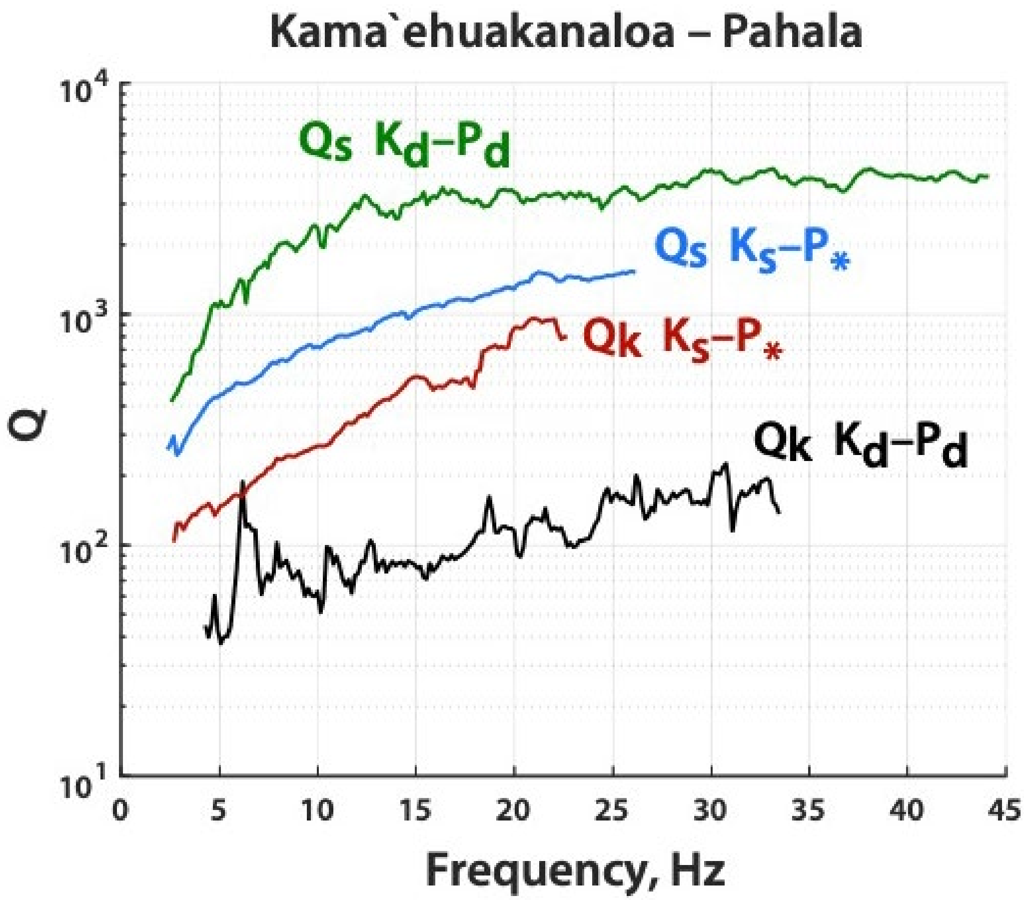

Figure 6. The bulk Q_K and shear Q_S are isolated for the path segments between Kama‘ehuakanaloa and Pāhala, for both shallow (<12 km, subscript s or *) and deep (subscript d) pathways (>30 km). In this comparison, the shallow Pāhala data are for the earthquake at Pāhala*. Note that the Q values are now plotted logarithmically along the vertical axis to permit the dynamic range in the data. As elsewhere, $Q_K < Q_S$. The bulk Q_K for deep paths diverge more substantially from Q_S from comparable shallow paths.

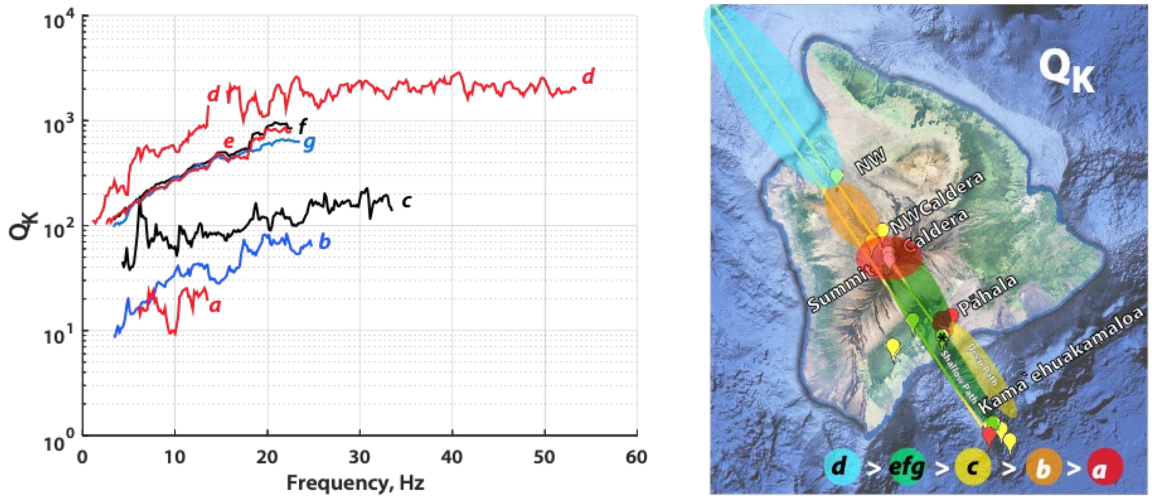

Figure 7. [Left] Q_K transect maps (Figures 2–6) are subdivided into a hierarchy of segmented Q_K measurements. The letters indicate the segments in common with Q_K and Q_S: Caldera-Summit (a), NWC–NW (b), Kd–Pd (c), NW–ACO (d), Ks–P* (e), Ks–NWC (f), P*–NWC (g). Segment naming includes: Mauna Loa Northwest (NW), Northwest of Caldera (NWC), Kama‘ehuakanaloa (Kd deep, Ks shallow), Pāhala (Pd deep, P* shallow). [Right] Regional Q_K measured for the linear segments—painted corresponding to $Q_K(f)$ values shown in the [Left]. The colored circle legend independently ranks Q_K from highest Q (cyan) > green > yellow > orange > lowest Q (red). NOTE that Figures 7 and 8 are independently scaled and color-coded.

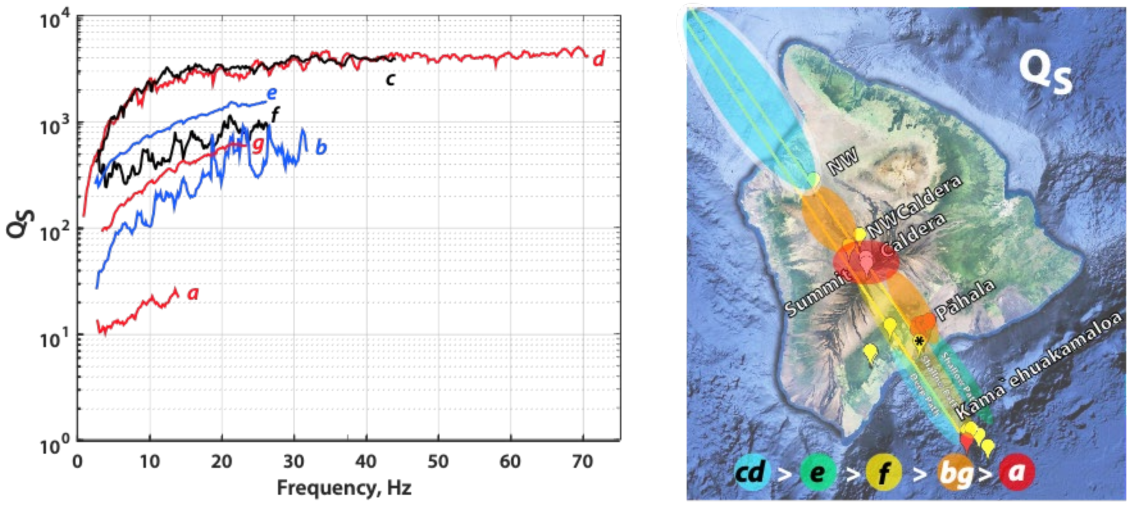

Figure 8. [Left] Q_S transect maps (Figures 2–6) are subdivided into a hierarchy of segmented Q_S measurements The letters indicate the segments in common with Q_K and Q_S following the nomenclature of Figure 7. [Right] Regional Q_S measured for the linear segments—painted corresponding to $Q_S(f)$ values shown in the [Left]. The colored circle legend independently ranks Q_S from highest Q (cyan) > green > yellow > orange > lowest Q (red). NOTE that Figures 7 and 8 are independently scaled and color-coded.

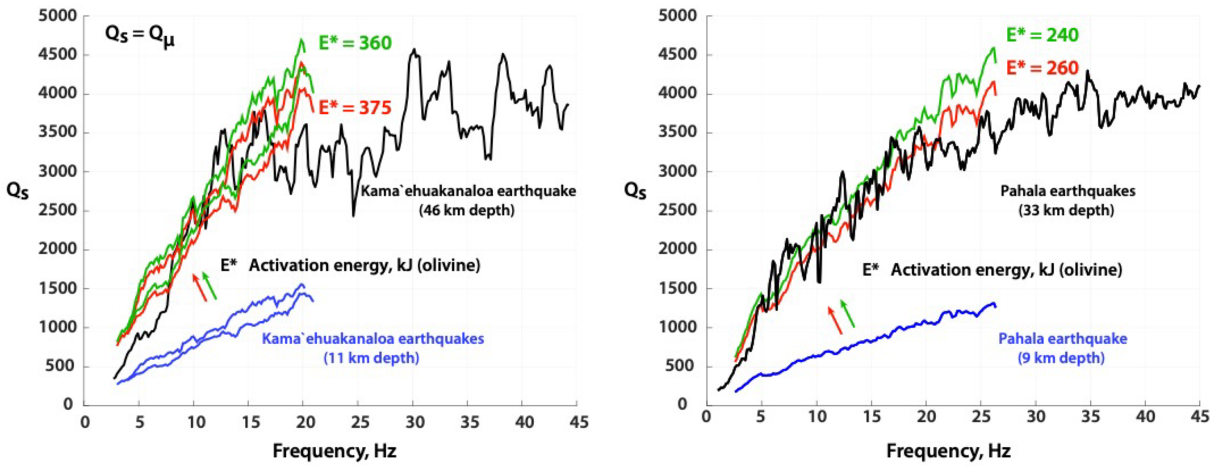

Figure 9. The effect upon Q_S for a fixed activation energy E^*, and the temperature and pressure range for earthquake hypocenters. [Left] The 46 km deep Kama‘ehuakanaloa event is compared with two shallow events at 11 km. These three spectra have nearly identical Q_P and thereby common source characteristics. The range of E^* is 360–375 kJ/mol. The fit to the deep Kama‘ehuakanaloa earthquake diverges above about 15 Hz, with Q_S decreasing—suggesting a different attenuation mechanism becomes active, producing a smaller Q_S. [Right] The 12 Pāhala deep events (>30 km) have a mean depth of 33±1.3 km, and are stacked and compared with the Pāhala* shallow event (M_L 4.9, 8.8 km). In this case the Q_S trend is matched by an E^* between 240 and 260.

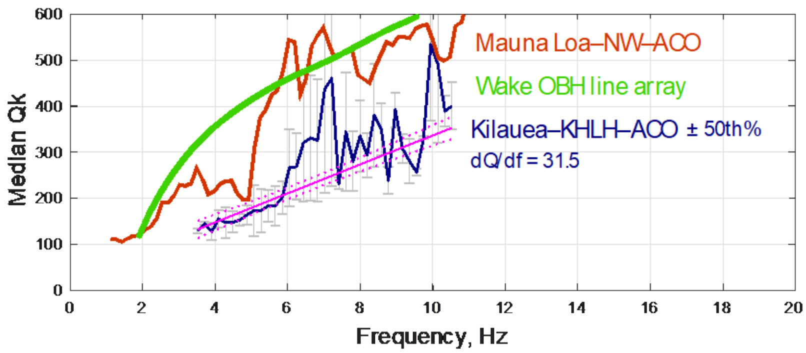

Figure 10. Q_K is plotted from three propagation paths at low frequency (< 11 Hz) and highest attenuation. The current study from NW Hawai‘i to ACO is shown in red. The path segment from Kahului, Maui to ACO (Butler 2020) is plotted in dark violet, with a linear trend where dQ/df ~ 32. The error bars show median absolute deviations (50th percentile) from the median. The Q_K green trend comes from the Butler et al. (1987) study near Wake Island—and has been abridged to the frequency range of the Kīlauea and Mauna Loa low frequency observations. From about 15–55 Hz the NW–ACO (d, Figure 7 [Left]) curve for Q_K flattens to ~2000, where the break in slope may reflect a change in the underlying Q_K mechanism. The Wake Island data extends to ~20 Hz and Q_K ~1000.

.

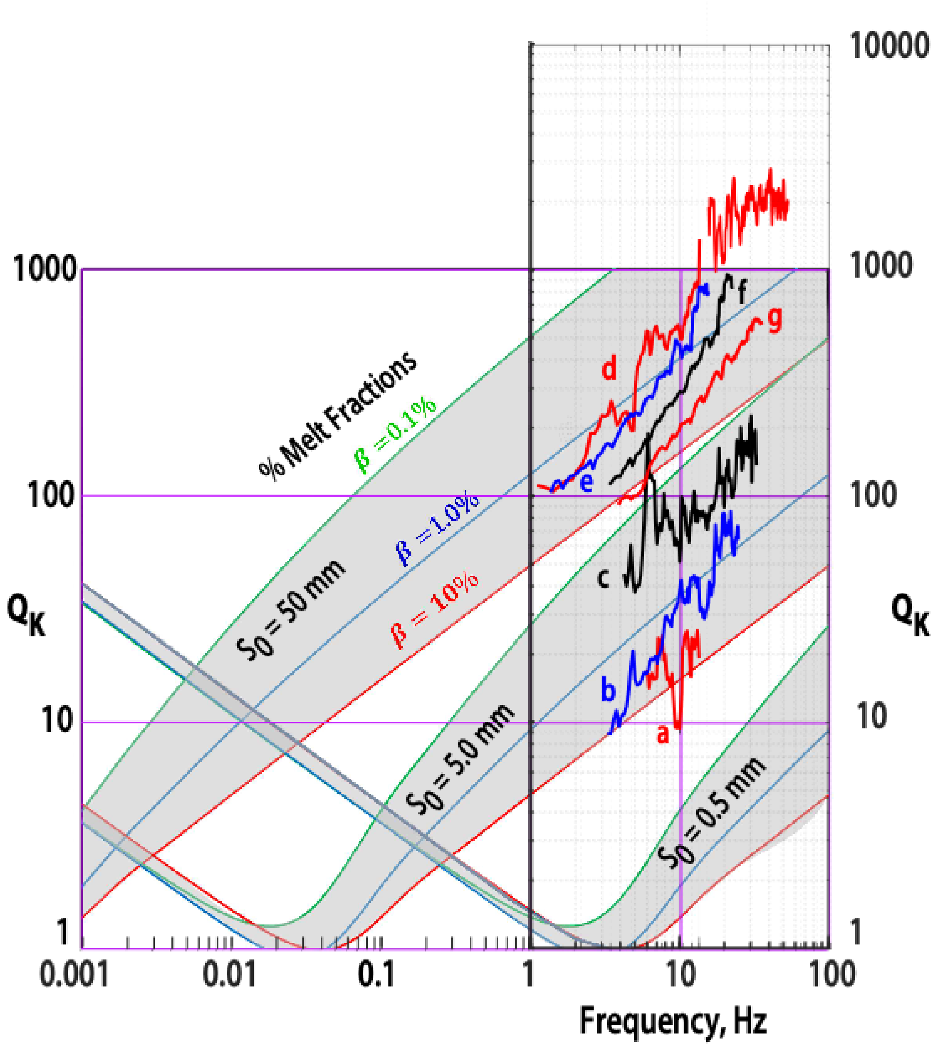

Figure 11. Q_K versus frequency for different melt fraction values β = 0.1% (green), 1.0% (blue), and 10% (red) and Clausius-Clapeyron slope value α = 5 MPa/K°. Shaded regions show Q_K values for S_0 = 0.5 mm, 5.0 mm, and 50.0 mm, where S_0 is the cell model for spherical melt inclusions in partially melted rocks. Between 1 and 100 Hz, the Q_K from Figure 7 are plotted in log-log format. For Q_K from the low attenuation transects (e, f, g), the large Q_K fall within the cell size S_0 = 50.0 mm with melt fractions of β = 1.0% to 10%. Note that although the transect (d) fits with (e, f, g), an alternate explanation due to vesicular basalts has already been proffered. For Q_K from the high attenuation transects (a, b, c), the small Q_K fall within the cell size S_0 = 5.0 mm with melt fractions of β = 0.1% to 10%. Figure adapted with permission from Lyakhovsky et al. (2021).

Supplement Appendix A.

Seismic bulk and shear attenuation along a transect from Kama‘ehuakanaloa volcano through Mauna Loa to the Aloha Cabled Observatory: Implications for the distribution of partial melt

Rhett Butler[1]

[1]Hawai‘i Institute for Geophysics and Planetology, School of Ocean and Earth Science and Technology, University of Hawai‘i at Mānoa, 1680 East-West Road, POST 602, Honolulu, HI 96822.

Supplement Appendix A comprises:

Earthquake Data Observed at Aloha Cabled Observatory (ACO)

Tables A1 and A2

Figure A1

Earthquake source spectrum

Text

Figures A2–A4

Path *Q* segmentation

Text

Figures A5–A6

Earthquake Data Observed at Aloha Cabled Observatory (ACO)

Table A1. Earthquake dataset

origin_time	latitude	longitude	depth	mag	km2ACO
2011-11-20T20:17:20.396Z	19.55	-155.623	10.2	4	432.2
2014-10-13T04:43:51.187Z	19.149	-155.588	3.2	4	471.5
2015-05-09T12:18:48.413Z	19.144	-155.583	2	4.5	472.3
2016-09-06T14:25:57.338Z	19.451	-155.598	0.8	4.1	442.7
2018-05-05T00:37:10.192Z	19.181	-155.406	8.8	4.9	478.9
2018-10-14T11:39:52.210Z	18.872	-155.234	11	3.87	517.6
2020-05-11T21:59:03.110Z	18.877	-155.22	11	3.94	517.9
2021-12-25T06:59:11.330Z	18.856	-155.192	10.9	3.92	521.4
2023-03-27T04:39:16.340Z	18.816	-155.16	7.8	4.12	527
2019-04-14T03:09:02.680Z	19.742	-155.791	13.3	5.3	404.6
2019-08-22T14:33:30.360Z	18.838	-155.237	46	4.18	520.5
2020-08-01T20:03:07.560Z	19.24	-155.413	31.7	4.2	473.1
2020-12-04T17:44:24.580Z	19.513	-155.663	4.7	4.1	433.3
2021-04-03T21:15:22.400Z	19.238	-155.514	7.9	4.3	467.4
2021-06-03T04:44:32.360Z	18.865	-155.236	10.8	4.02	518.1
2021-06-18T02:32:04.670Z	19.23	-155.402	32.7	4.5	474.6
2021-08-18T12:01:58.880Z	19.214	-155.393	32.9	4.1	476.6
2021-10-06T06:36:56.410Z	19.226	-155.398	32.7	4.6	475.3
2021-12-24T11:31:34.390Z	18.87	-155.234	11.9	4.87	517.7
2022-01-04T00:13:26.770Z	19.216	-155.4	33.5	4.3	476
2022-01-31T11:54:32.360Z	19.219	-155.396	32.8	4	476
2022-07-27T03:46:04.880Z	19.226	-155.392	34	4.3	475.5
2022-07-27T04:28:14.180Z	18.85	-155.236	10.6	4.62	519.5
2022-08-23T05:11:30.110Z	19.201	-155.391	31.8	4	478
2022-09-06T00:23:12.610Z	19.253	-155.369	32.9	4	474.5
2022-09-08T12:04:03.510Z	19.239	-155.392	32.9	4.2	474.4
2022-11-28T08:56:25.740Z	19.471	-155.601	-1.2	4.2	440.7

2023-05-08T09:58:58.600Z	19.24	-155.374	32	3.8	475.4
2022-06-19T21:15:18.230Z	19.241	-155.399	33.1	3.9	473.8
2021-09-12T11:45:06.430Z	19.221	-155.417	36.2	3.8	474.6

Table A2. Earthquake mean ± σ for depth, *P* and *S* apparent group velocities

Earthquake locations	depth, km	± km	Vp, km/s	± km/s	Vs, km/s	± km/s
Kamaʻehuakanaloa	10.6	1.3	7.7	0.3	4.6	0.2
Kamaʻehuakanaloa deep	46.0		7.9		4.6	
Pāhala	5.5	3.4	7.7	0.3	4.4	0.1
Pāhala*	8.8		7.3		4.3	
Pāhala deep	33.2	1.3	7.9	0.03	4.6	0.04
Mauna Loa NW near caldera	7.5	3.9	7.7	0.1	4.5	0.1
Mauna Loa caldera	-0.2	1.4	7.5	0.2	4.3	0.02
NW (northwest)	13.3		7.9		4.5	

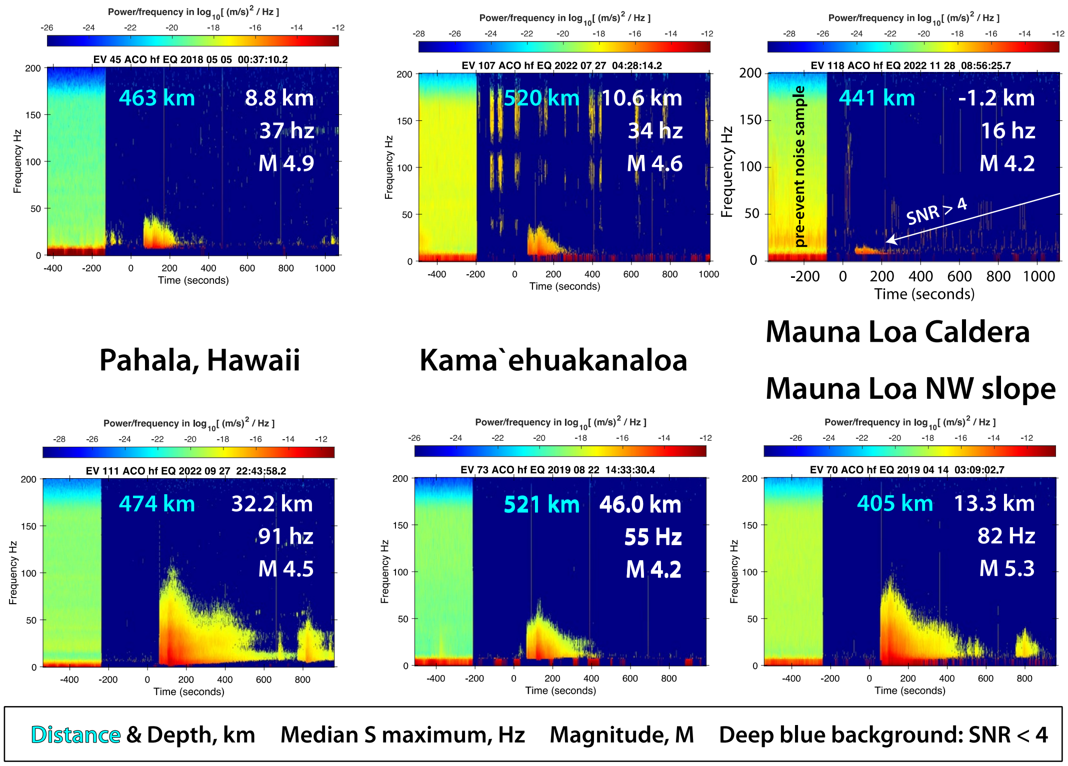

Figure A1. ACO spectrograms (frequency-time plots) are shown for six events in this study—left Pāhala, center Kamaʻehuakanaloa, and right Mauna Loa. The Pāhala* earthquake from Figure 1 is plotted in the upper left. The legend is at the base. The color bars show signal power. The left portion of each spectrogram shows the pre-event noise level. The deep blue field shows the frequency-time area where signal-to-noise (SNR) < 4. The earthquakes show only data meeting the SNR > 4 criterion. It is significant that shear wave energy from one of the Pāhala earthquakes at 474 km distance from ACO expressed frequencies up to 91 Hz, implying a high Q_S shear wave pathway through, beneath Mauna Loa. From within Mauna Loa Caldera frequencies are limited up to 16 Hz. At distances of 400 –550 km, high signal-to-noise (SNR > 4) waveform data are available for the differing volcano distances, depths, M_L and peak frequencies.

Earthquake source spectrum

Since our effective *Q* determinations are only as good as the spectral model employed, I took the effort to confirm that the earthquakes *conformed* to the expectations of the source model in deriving *Q*. Figure A2 plots two examples of spectral measurements fits between the source model and data for two deep Pāhala earthquakes. The Pāhala event in Figure A2 [A,B] *conforms* to the ω^{-2} source spectrum for *P*- and *S*-waves. However, the Pāhala earthquake *S*-wave shown in Figure A2 [D] is *non-conforming*, as the data exceed the source model near 1 Hz. Figure A3 compares *conforming* and *non-conforming* spectra for deep events near Pāhala. Figure A4 plots the location of off-shore, deep *non-conforming* earthquakes

In reviewing the source spectra trend note that an ω^{-4} trend (dashed cyan) first seen by Butler (2018) for high-frequency events north of Molokaʻi is again observed in Figure A2 for both *P*- and *S*-waves. An apparent corner of the ω^{-4} at 1.5 Hz is shown for illustration only. The reader is referred to Butler (2018) for implications and discussion.

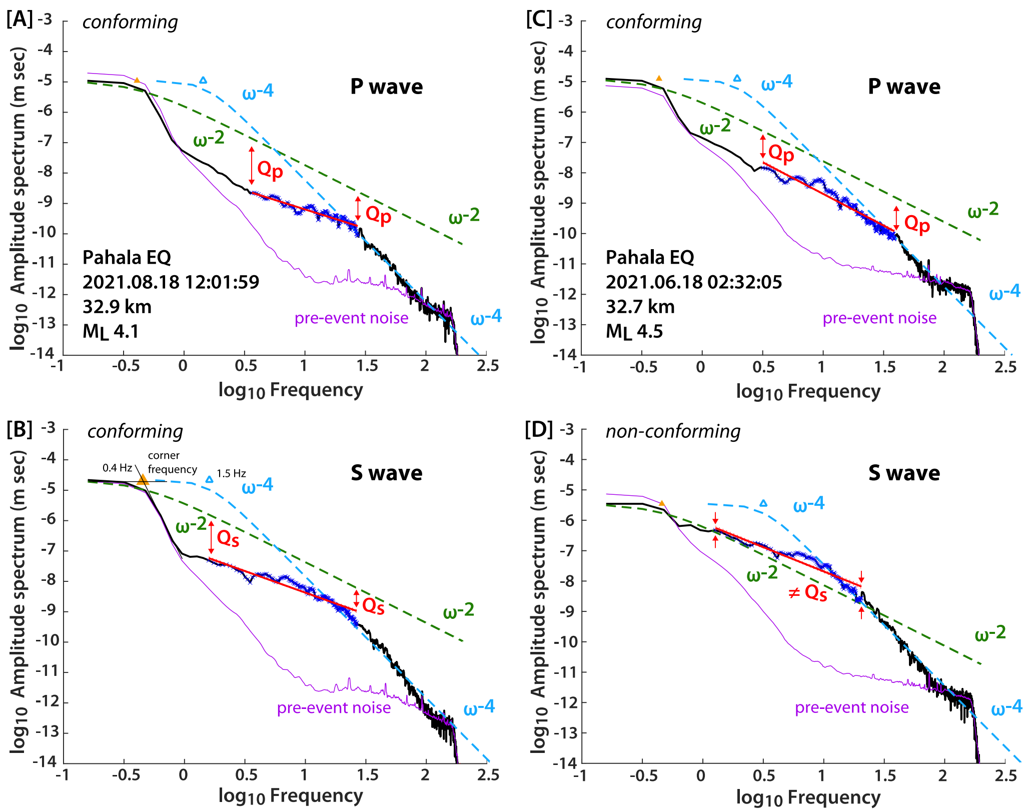

Figure A2. The elements of the Q measurement technique are shown for two Pāhala deep earthquakes. [B] The corner frequency (0.4 Hz) is measured at the extrapolated intersection of the amplitude spectral slope with the low frequency peak value (e.g., Hanks and Thatcher, 1972).

The ω^{-2} source model (dashed green) exceeds the data (blue) over a frequency band (red), whose offset is related to Q. Note in [D] that the source ω^{-2} amplitude spectrum (dashed green) is smaller than the data (blue), and thereby does not *conform* with the source model. In reviewing the earthquake spectra of all events analyzed, only some of the deep S wave data were observed to be *non-conforming*. All shallow earthquake data were *conforming*.

Hanks, T.C. & Thatcher, W., 1972. A graphical representation of seismic source parameters, J. Geophys. Res., 77(23), 4393–4405.

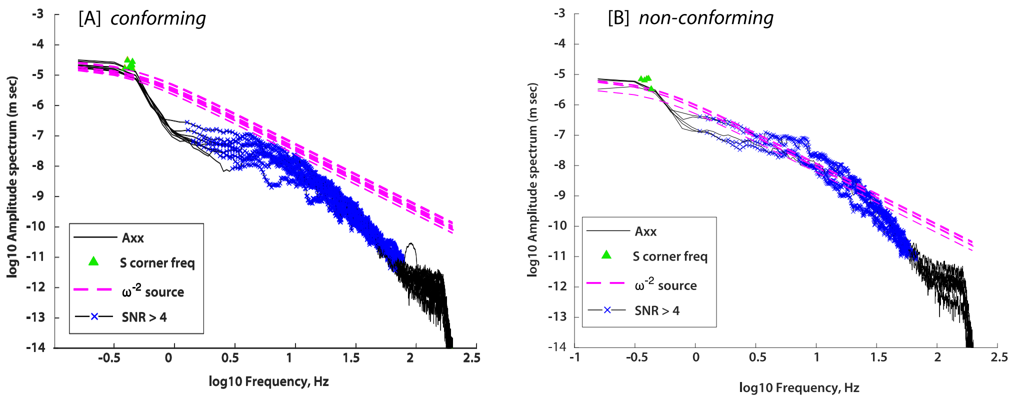

Figure A3 [B] Several *non-conforming* deep earthquakes near Pāhala show amplitude spectra (*Axx*) that exceed the source model amplitude fall-off rate (ω^{-2} shown as magenta) appropriate for the measured corner frequency (green triangles). [A] Selected plots of amplitude spectra for Pāhala deep earthquakes which *conform* to the ω^{-2} source model. Only data (blue 'x') with SNR > 4 are plotted on along the *Axx* traces (black). The downward offset of *non-conforming* corner frequencies with respect to *conforming* earthquakes may represent theoretical earthquake source effects discussed in Kaneko and Shearer (2014, 2015). Note that of the 16 deep Pāhala events, only 4 showed *non-conforming S* wave spectra, whereas *all P* wave spectra and *all* shallow earthquakes in the data set were found to be *conforming*.

Kaneko, Y., and P. M. Shearer (2014). Seismic source spectra and estimated stress drop derived from cohesive-zone models of circular subshear rupture, Geophys. J. Int. 197, no. 2, 1002–1015.

Kaneko, Y., and P. M. Shearer (2015). Variability of seismic source spectra, estimated stress drop, and radiated energy, derived from cohesive-zone models of symmetrical and asymmetrical circular and elliptical ruptures, J. Geophys. Res. 120, no. 2, 1053–1079.

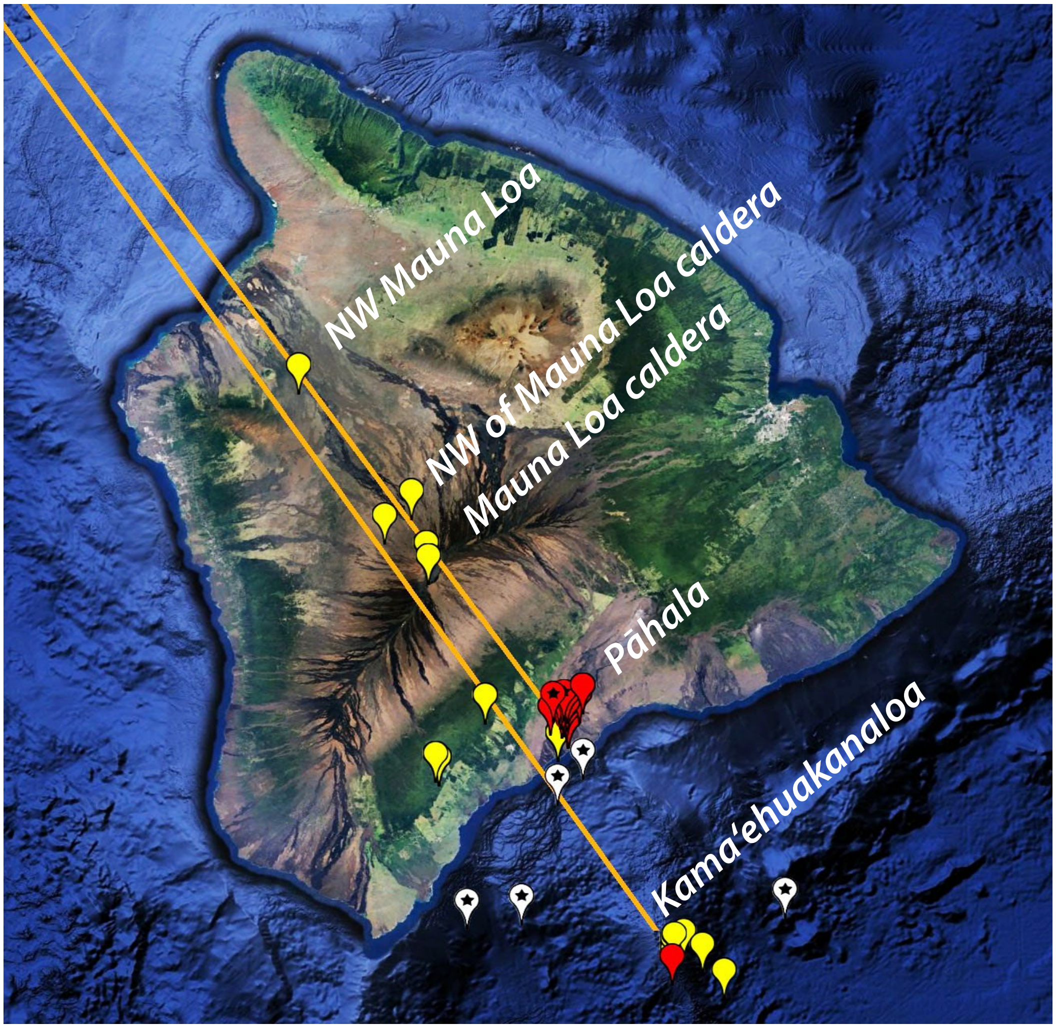

Figure A4. Map of Hawaiʻi island showing earthquake locations: (red) events >30 km depth; (yellow) events <12 km; (white) supplemental, off-shore deep earthquake sources. Symbols with a ★ indicate earthquake data that *do not conform* with the ω^{-2} Brune (1970) source model. Only one of the four deep Pāhala *non-conforming* earthquakes are visible in the cluster of red events. Orange lines show propagation paths to ACO (see Figure 1).

Brune, J. N. (1970). Tectonic stress and the spectra of seismic shear waves from earthquakes, J. Geophys. Res. 75, no. 26, 4997–5009.

Path *Q* segmentation

When (1) path *Q*'s are similar, and (2) when their differences are less than the spectral noise, the path segmentation may be derived.

Consider the pathway Kamaʻehuakanaloa ⟶ Caldera:

$$\frac{\Delta t_{Kama\rightarrow ACO} - \Delta t_{Caldera\rightarrow ACO}}{Q_{Kama\rightarrow Caldera}} = \frac{\Delta t_{Kama\rightarrow ACO}}{Q_{Kama\rightarrow ACO}} - \frac{\Delta t_{Caldera\rightarrow ACO}}{Q_{Caldera\rightarrow ACO}} \qquad \text{(a1)}$$

$$\text{Let } Q_{Kama\rightarrow ACO} \approx Q_{Caldera\rightarrow ACO} \approx Q_0 \approx \frac{Q_{Kama\rightarrow ACO} + Q_{Caldera\rightarrow ACO}}{2} \qquad \text{(a2)}$$

Then,

$$\frac{\Delta t_{Kama\rightarrow ACO} - \Delta t_{Caldera\rightarrow ACO}}{Q_{Kama\rightarrow Caldera}} \approx \frac{\Delta t_{Kama\rightarrow ACO}}{Q_0} - \frac{\Delta t_{Caldera\rightarrow ACO}}{Q_0} \qquad \text{(a3)}$$

$$\frac{\Delta t_{Kama\rightarrow ACO} - \Delta t_{Caldera\rightarrow ACO}}{Q_{Kama\rightarrow Caldera}} \approx \frac{\Delta t_{Kama\rightarrow ACO} - \Delta t_{Caldera\rightarrow ACO}}{Q_0} \qquad \text{(a4)}$$

Therefore…

$$Q_{Kama\rightarrow Caldera} \approx Q_0 \qquad \text{(a5)}$$

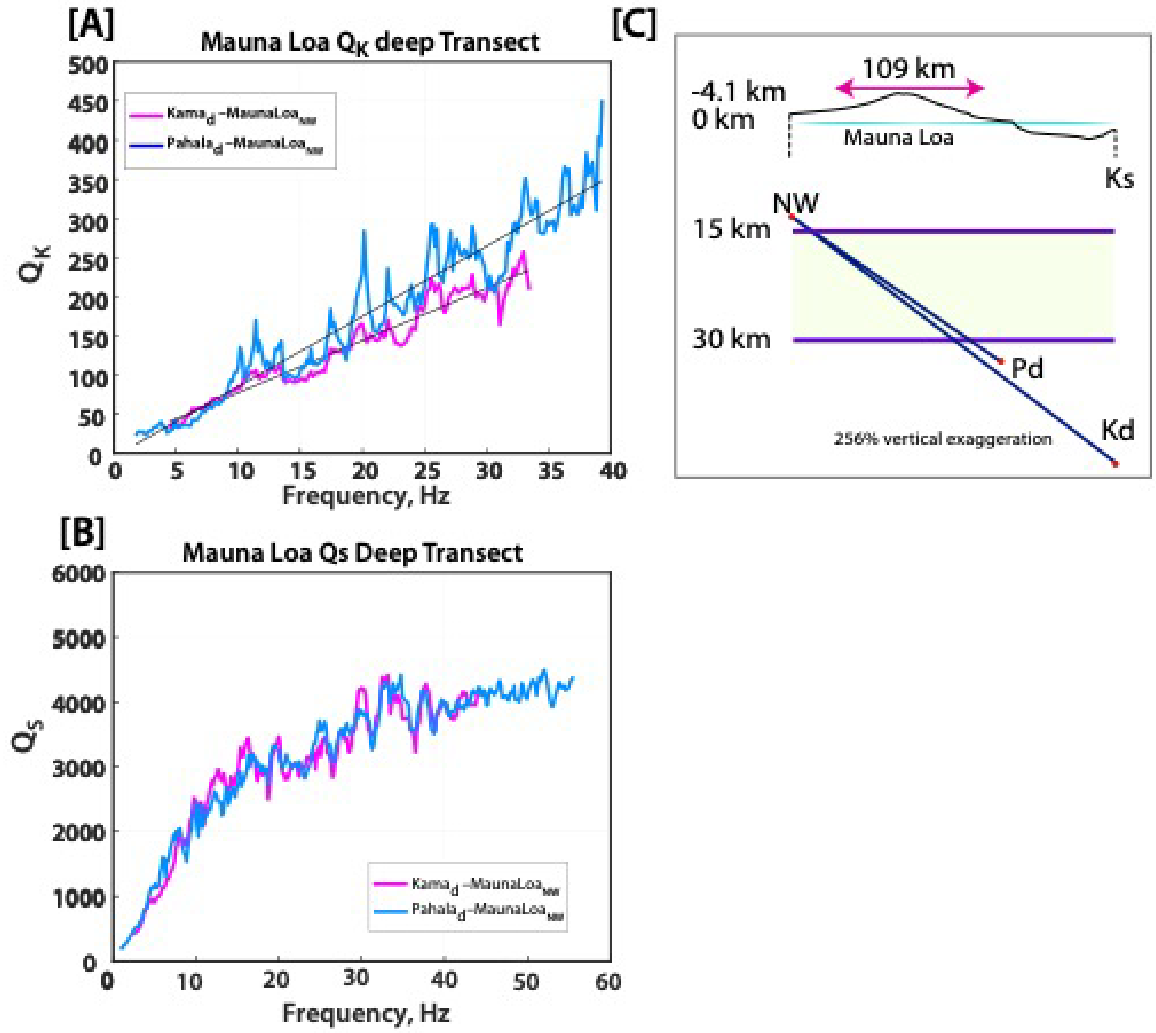

Figure A5. Adapted from Figure 3 showing only the deep paths to present a clear comparison. Although the comparisons are *not* perfect, there is a clear tendency–surprisingly–for peaks and troughs to align. This suggests that the deep propagation paths to NW from Pāhala and Kamaʻehuakanaloa are similar. The simple cartoon illustrates [C] the proximal propagation.

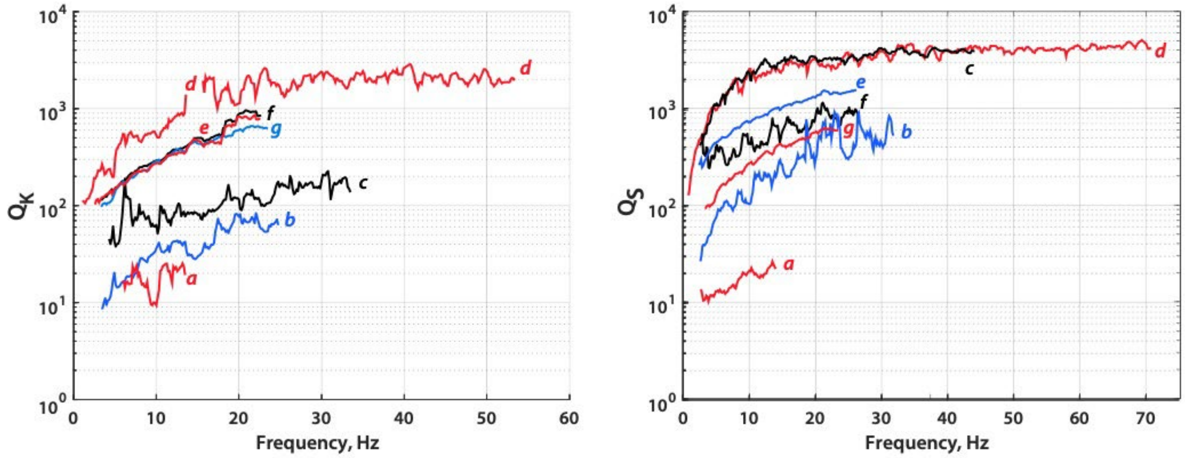

Figure A6. The Mauna Loa transect maps (Figures 2–6) are subdivided into a hierarchy of segmented Q measurements. Q_K is the left panel, Q_S is right. The letters indicate the segments in common with Q_K and Q_S following the nomenclature of Figure 7. Q traces are colored for visual clarity, and are not necessarily consistent between the left and right panels.

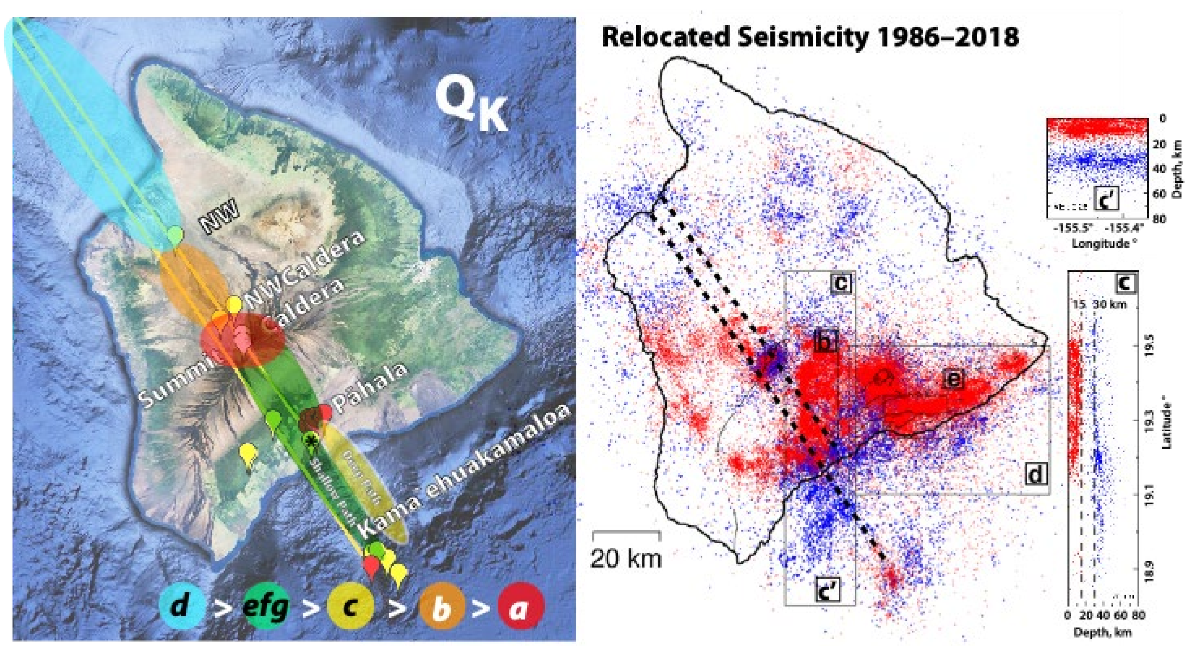

Figure 12. [Left] Regional Q_K variations are shown and annotated from Figure 7. [Right] Relocated seismicity in 1986–2018 are shown from the study of Matoza et al., (2020), where rectangular regions are included from their presentation—noted by letters within squares ☐.

Only region ‘**c**’ overlaps significantly with the Q_K data between the Mauna Loa and Kama‘ehuakanaloa calderas, roughly centered on Pāhala. Seismicity is projected onto vertical, length-wise ‘**c**’ and width-wise ‘**c**′’ cross-sections (far right). Note in ‘**c**’ the dashed lines plotting 15 and 30 km depths, which adjoin the shallow and deeper seismicity—between these lines are significantly fewer earthquakes. Figure 3[D] shows the propagation paths transecting this zone. NOTE that Figures 7 (Q_K) and 8 (Q_S) are independently scaled and color coded. Figure adapted from Matoza et al. (2020).